International Journal of Heat and Mass Transfer 77 (2014) 1213–1230

Contents lists available at ScienceDirect

International Journal of Heat and Mass Transfer

journal homepage: www.elsevier.com/locate/ijhmt

Micro-channel evaporator for space applications – 1. Experimental pressure drop and heat transfer results for different orientations in earth gravity

Hyoungsoon Lee [a], Ilchung Park [a], Issam Mudawar [a,*], Mohammad M. Hasan [b]

[a] Purdue University Boiling and Two-Phase Flow Laboratory (PU-BTPFL), School of Mechanical Engineering, 585 Purdue Mall, West Lafayette, IN 47907, USA
[b] NASA Glenn Research Center, 21000 Brookpark Road, Cleveland, OH 44135, USA

ARTICLE INFO

Article history:
Received 29 January 2014
Received in revised form 2 June 2014
Accepted 3 June 2014
Available online 1 July 2014

Keywords:
Flow boiling
Micro-channel
Pressure drop
Flow orientation
Reduced gravity

ABSTRACT

Boiling and condensation are being considered for operation of thermal control systems (TCSs) in future space vehicles to capitalize upon their high heat transfer coefficients and appreciable reduction in TCS weight and volume. A primary concern in designing these systems is a lack of technical knowhow on the influence of buoyancy and therefore body force on two-phase heat transfer in reduced gravity. In particular, there is keen interest in developing predictive tools for pressure drop and heat transfer and identifying the minimum coolant flow rate that would negate the influence of body force. Two-phase flow in micro-channels provides unique advantages to space systems by greatly increasing flow inertia for a given flow rate, which helps resist body forces effects. This study is the first part of a two-part study addressing the effectiveness of two-phase micro-channels at negating body force effects. Flow boiling experiments are conducted with FC-72 in a test module containing 80 of 231 μm wide × 1000 μm deep micro-channels in three different flow orientations: horizontal, vertical upflow and vertical downflow over broad ranges of mass velocity and heat flux. Also investigated are conditions that trigger two different types of two-phase flow instability. In addition, different flow regimes are identified with an aid of high-speed video imaging, and the flow regime data are compared to an exiting flow regime map and used to develop new relations for transition boundaries between regimes. Overall, the present study proves the existence of a mass velocity threshold above which identical heat transfer performances are achieved regardless of orientations.

1. Introduction

1.1. Phase change cooling schemes

Developments in many modern applications are becoming increasingly dependant on the ability to dissipate large amounts of heat from small surface areas. Examples include computer data centers, avionics, hybrid vehicle power electronics, and laser and microwave military systems [1]. Achieving the heat dissipation requirements for these and other applications has spurred significant interest in transitioning from present air cooling and single-phase liquid cooling schemes to boiling. Liquid-to-vapor change of phase promises remarkable increases in the heat transfer coefficient. Additionally, boiling can be implemented in a variety of configurations, including pool boiling [2–5], channel flow boiling [6–8], jet [9–12] and spray [13–16], as well as with enhanced surfaces [17–19] and hybrid cooling configurations [20]. At the system level, heat dissipation by boiling demands heat rejection schemes that provide commensurate heat transfer coefficients, which are possible mostly with condensation [21].

Of the different boiling schemes, micro-channel flow boiling has gained unprecedented popularity because of both outstanding heat transfer performance and system advantages, including compact and lightweight design and small coolant inventory. As discussed in [1], this cooling scheme capitalizes on the advantages of flow boiling in channels ranging in hydraulic diameter from about 50 to 1000 μm. But the same study points to a unique advantage of micro-channel flow boiling for space applications. For a given coolant mass flow rate, reducing hydraulic diameter greatly increases flow velocity, imparting the cooling system with substantial resistance to changes in body force in space systems. These systems encounter large fluctuations in body force (*e.g.*, Earth gravity, Lunar

* Corresponding author. Tel.: +1 (765) 494 5705; fax: +1 (765) 494 0539.
E-mail address: mudawar@ecn.purdue.edu (I. Mudawar).
URL: https://engineering.purdue.edu/BTPFL (I. Mudawar).

http://dx.doi.org/10.1016/j.ijheatmasstransfer.2014.06.012
0017-9310/

Nomenclature

C_c	contraction coefficient
c_p	specific heat at constant pressure
D_h	hydraulic diameter
f	Fanning friction factor
G	mass velocity
H	distance normal to flow direction
h	heat transfer coefficient
H_{ch}	height of micro-channel
h_{fg}	latent heat of vaporization
H_p	height of inlet/outlet plenums
j_g^*	modified superficial vapor velocity
j_k	superficial velocity for phase k ($k = g$ or f)
k	thermal conductivity
L	length
m	fin parameter
$\dot{m}$	mass flow rate per micro-channel
N_{ch}	number of micro-channels
P	pressure
P_{crit}	critical pressure
P_R	reduced pressure, $P_R = P/P_{crit}$
Pr	Prandtl number
q	heat transfer rate
q''	heat flux
q''_{eff}	effective heat flux based on width of unit cell containing single micro-channel
Re	Reynolds number
T	temperature
$T_{w,b}$	micro-channel bottom wall temperature
ΔT_d	subcooling at axial location of bubble detachment
u^*	friction velocity
v	specific volume
W_{ch}	width of single micro-channel
W_p	width of inlet/outlet plenums
W_W	width between micro-channels
We^*	modified Weber number
x	flow quality
x_d	thermodynamic equilibrium quality at axial location of bubble detachment
x_e	thermodynamic equilibrium quality
X_{tt}	Lockhart-Martinelli parameter for turbulent liquid and turbulent vapor flows
Y_B	distance from wall to tip of vapor bubble
z	stream-wise coordinate

Greek symbols

α	void fraction
β	aspect ratio (W_{ch}/H_{ch})
η	fin efficiency
μ	dynamic viscosity
ρ	density
σ	surface tension
σ_c	contraction ratio
τ	shear stress
ϕ	two-phase pressure drop multiplier

Subscripts

A	accelerational
b	bottom thermocouple plane
c	contraction
e	expansion, thermodynamic equilibrium
F	frictional
f	liquid, bulk fluid
fo	liquid-only
G	gravitational
g	vapor
H	heated perimeter of micro-channel
in	inlet
out	outlet
p	plenum
s	solid
sat	saturation
sp	single phase
sub	subcooling
t	top thermocouple plane
tot	total
tp	two-phase
w	wall

gravity, Martian gravity, microgravity), and a performance independent of gravitational environment is crucial to achieving predictable and reliable operation. This attribute is the primary motivation for the present study.

1.2. Body force influence on flow boiling

The influence of body force on fluid motion and therefore heat transfer in flow boiling systems is dictated by the magnitude of buoyancy force relative to other forces such as inertia and surface tension. Because of large density difference between phases, buoyancy can play a crucial rule in a flow boiling system. The primary concern in designing a two-phase thermal management system for a space mission is the lack of technical knowhow concerning the influence of buoyancy in reduced gravity. Absent a detailed understanding of this influence, designers of thermal management systems for space missions are primarily interested in operating conditions that negate the influence of reduced gravity. While very high coolant velocities are key to achieving this goal, such velocities greatly increase pressure drop and pumping power, resulting in adverse effects on thermodynamic efficiency of the cooling system. Furthermore, achieving very high velocities may not be possible given the stringent power budget of a space system. A more achievable goal is to determine the *minimum* coolant flow rate that can negate the influence of reduced gravity.

The influence of microgravity on flow boiling can be assessed by conducting experiments in a variety of platforms, including drop tower, drop shaft, sounding rocket, parabolic flight, space shuttle and the International Space Station (ISS) [22]. However, most phase change studies conducted since the 1960 have been focused on pool boiling [23], with only a handful dedicated to the study of flow boiling. For example, Saito et al. [24] conducted parabolic flight experiments involving saturated and subcooled water flow along the surface of an 8 mm rod heater centrally located along a 25×25 mm^2 transparent channel. Bubbles were observed to slide along the heater rod without the detachment often observed in Earth's gravity. Differences in vapor behavior between Earth's gravity and microgravity were more pronounced at lower velocities, higher heat fluxes and lower liquid subcoolings, yet these differences did not influence the local heat transfer coefficient. Ma and Chung [25,26] examined flow boiling of FC-72 at speeds of 0 to 0.3 m/s along a 2.54×2.54 cm^2 gold-film heated wall in a 1 s drop tower. Bubble size was observed to decrease monotonically with increasing velocity, which suggests that high velocities might negate the effects of gravity on bubble nucleation, growth and departure. Ohta [27] conducted both pool boiling and flow

boiling experiments using R113, water and ethanol in both Earth gravity and microgravity, and found that the heat transfer coefficient in moderate quality annular flow was reduced by 7% in microgravity and enhanced by 25% at $2g_e$ compared to Earth gravity. However, gravity effects were absent at high velocities in high quality annular flow, and in very low quality flow where heat transfer is dominated by nucleate boiling. Zhang et al. [28] conducted parabolic flight experiments with FC-72 to assess the influence of reduced gravity on flow boiling critical heat flux (CHF). They showed that CHF at low velocities in microgravity is significantly smaller than in horizontal flow on Earth, but CHF differences between the two environments decreased with increasing velocity, culminating in virtual convergence at about 1.5 m/s. This finding proved that it is possible to design inertia-dominated systems by maintaining flow velocities above the convergence limit. Observing this limit allows data, correlations and models obtained from experiments conducted in Earth gravity to be safely implemented in the design of space systems.

Another method to assessing the influence of body force on flow boiling is to conduct experiments on Earth involving different orientations to create a fractional g-field perpendicular to the heated wall. This method overcomes the short duration limits of drop tower, drop shaft and parabolic flight experiments, and high cost of space shuttle and ISS experiments. But changing flow orientation is not a precise method to simulating reduced gravity since another component of body force is prevalent parallel to the heated wall. Several studies have examined the influence of orientation on flow boiling heat transfer [29–32]. These studies showed that vapor motion in a vertical downflow switches from concurrent relative to the liquid velocity for high inlet liquid velocities to countercurrent at low velocities. Zhang et al. [23,33] examined the influence of flow orientation for FC-72 with subcooled inlet conditions in a rectangular channel that was heated along one side. They observed a variety of complex flow regimes depending on the combined effects of flow velocity, flow orientation, and placement of the heated wall relative to gravity. The influence of orientation was significant only at low inlet liquid velocities, where buoyancy is dominant. Overall, low velocities produced CHF values for certain orientations that were much smaller than those for vertical upflow. However, orientation effects were virtually eliminated above a threshold velocity and virtually identical CHF values were measured regardless of orientation. Recently, studies were conducted to extend the ground tests of Zhang et al. to saturated inlet conditions with finite vapor void [34–37]. The inlet void greatly increased liquid velocity along the flow channel, causing the influence of body force to be negated at lower mass velocities than for subcooled inlet conditions.

1.3. Objectives of study

The present study is part of NASA's Flow Boiling and Condensation Experiment (FBCE), which is projected for deployment in the International Space Station (ISS) in 2017 [38]. This project aims to amass flow boiling and condensation databases in microgravity, which would ultimately serve as foundation for development of mechanistic models and design tools for future space missions. Because of bubble stagnation along heated surfaces in microgravity, a key challenge in prior ISS two-phase experiments has been an inability to safely preheat the working fluid without incurring CHF. A micro-channel evaporator is deemed very effective at increasing flow velocity for a given flow rate, therefore aiding in removal of vapor bubbles and prevention of localized dryout. A micro-channel evaporator is also highly effective at removing the large amounts of heat dissipated from avionics in thermal control systems (TCSs) employed in space systems. A more detailed discussion on CHF mechanisms in small channels and means of achieving very high CHF is provided in [39–43].

The present two-part study will explore the influence of orientation on pressure drop and heat transfer associated with flow boiling in micro-channels. The influence of orientation is examined by performing identical tests in horizontal flow, vertical upward and vertical downflow. In the present part, the pressure drop and heat transfer characteristics and associated flow regimes are examined for different mass velocities and orientations. The second part [44] will examine predictive tools for pressure drop and heat transfer coefficient as well as criteria to negate the influence of body force for different gravitational environments.

2. Experimental methods

2.1. Flow boiling facility

Fig. 1(a) shows a schematic of the experimental apparatus that is used to deliver FC-72 to a micro-channel test module at the desired pressure, temperature and flow rate. FC-72 is a dielectric liquid with a relatively moderate saturation temperature at 1 bar of 56 °C. It is deaerated by simultaneous vigorous boiling and condensation in the loop's reservoir for a minimum of 30 min. The deaerated fluid is circulated with the aid of a magnetically driven Micropump gear pump. Exiting the pump, the liquid passes through a control valve followed by a particulate filter and a Flow Technology turbine flow meter. Prior to entering the test module, the liquid is heated to the desired temperature by a Hotwatt inline electrical pre-heater, which is controlled manually by a variac. Temperatures are measured at the inlet and outlet of the pre-heater and along the pre-heater's cartridge heater with type-T thermocouples. An Omega controller is programmed to cut-off electrical power input to the pre-heater should any of the pre-heater's temperatures exceed 150 °C. The electrical power input to the pre-heater is measured by a Yokogawa power meter. Throttling valves are mounted upstream and downstream of the test module. The two-phase mixture leaving the test module is routed to a liquid-to-air heat exchanger, where it is cooled down to near ambient temperature before returning to the reservoir.

2.2. Test module

Fig. 1(b) depicts the detailed construction of the test module. Four parallel sets of 20 micro-channels are machined into the 50.0 mm × 152.4 mm top surface of an oxygen-free copper block. Each micro-channel has a cross-section of 231 μm × 1000 μm ($W_{ch} \times H_{ch}$). Four Hotwatt cartridge heaters, which are connected electrically in parallel, are inserted into the bottom of the copper block to supply heat to the micro-channels. The cartridge heaters are powered by a single 20 A variac, which is connected to a Yokogawa power meter to measure electrical power input. The copper block is inserted into an insulating G-10 fiberglass plastic housing that features plenums at the inlets and outlets of the micro-channels to ensure uniform flow distribution. A second G-10 plate is used to resist heat loss on the underside of the copper block. The tops of the micro-channels are closed off with a transparent polycarbonate plastic cover plate, which also provides optical access to the flow in the micro-channels. The test module's parts are clamped together by threaded rods, trapping o-rings between the individual parts.

Type-E thermocouples are used to measure the temperature of working fluid in the inlet and outlet plenums of the test module, and the copper block at five axial locations of z = 12.7, 44.5, 76.2, 108.0 and 137.7 mm along the micro-channel length. Two thermocouples are mounted at each axial location, spaced 12 mm

(H_b = 12 mm) normal to the flow direction, with the upper thermocouple embedded 6 mm below of the bottom wall of the microchannels (H_t = 6 mm). The thermocouple pairs are used to determine heat flux at the five axial locations. Pressure is measured in the inlet and the outlet plenums using Honeywell absolute pressure transducers. All temperature, pressure, flow rate and power input signals are recorded using an NI SCXI-1000 data acquisition system.

Flow visualization is conducted with a Photron FASTCAM-Ultima high-speed video camera fitted with a Micro-Nikkor 105 mm f/2.8G lens to capture flow boiling regimes along the micro-channels. Video segments are recorded for up to 1 s at 8000 frames per second (fps) with a pixel resolution of 1024 × 256. Lighting for the video camera is provided by 16 of 5-W white LEDs that are fitted into a fan-cooled enclosure.

2.3. Test procedure and measurement accuracies

The flow boiling experiments are conducted at three different orientations: horizontal, vertical upflow and vertical downflow, to assess the influence of gravity on boiling behavior. For each orientation, experiments are conducted using the following procedure. The FC-72 is circulated through the loop and both the flow rate and test module inlet temperature gradually adjusted to the desired values. Then, by throttling the control valves situated upstream and downstream of the test module, the pressure at the inlet to the test module is ramped up to 2.0 bar. Once the temperature, pressure and flow rate are set to the desired operating conditions, the electrical power to the cartridge heaters in the test module is increased in small increments. Both the flow rate and inlet pressure are re-set following each power increment. As indicated in Table 1, six different flow rates are tested at each orientation, with three to six power inputs used per flow rate. Tests to measure the pressure drop and heat transfer coefficient are conducted separately. The heat transfer tests exclude those involving severe flow oscillations or where high uncertainty is encountered in determining the local heat transfer coefficient. A summary of the thermophysical properties of saturated FC-72 at T_{sat} = 78.6 °C, corresponding to the test module's inlet pressure of 2 bar, is provided in Table 2.

All system pressures are measured by Honeywell absolute pressure transducers having an accuracy of ±0.05%. The type-E thermocouples used to measure the test module's temperatures have an uncertainty of ±0.04%. The accuracy of the Flow Technology turbine flow meter is ±0.05%. The measurement accuracies of the Yokogawa power meters are ±0.1% and ±0.2%. Overall uncertainties in determining the local heat transfer coefficient for horizontal flow, vertical upflow and vertical downflow are 9.85%, 9.77% and 9.89%, respectively.

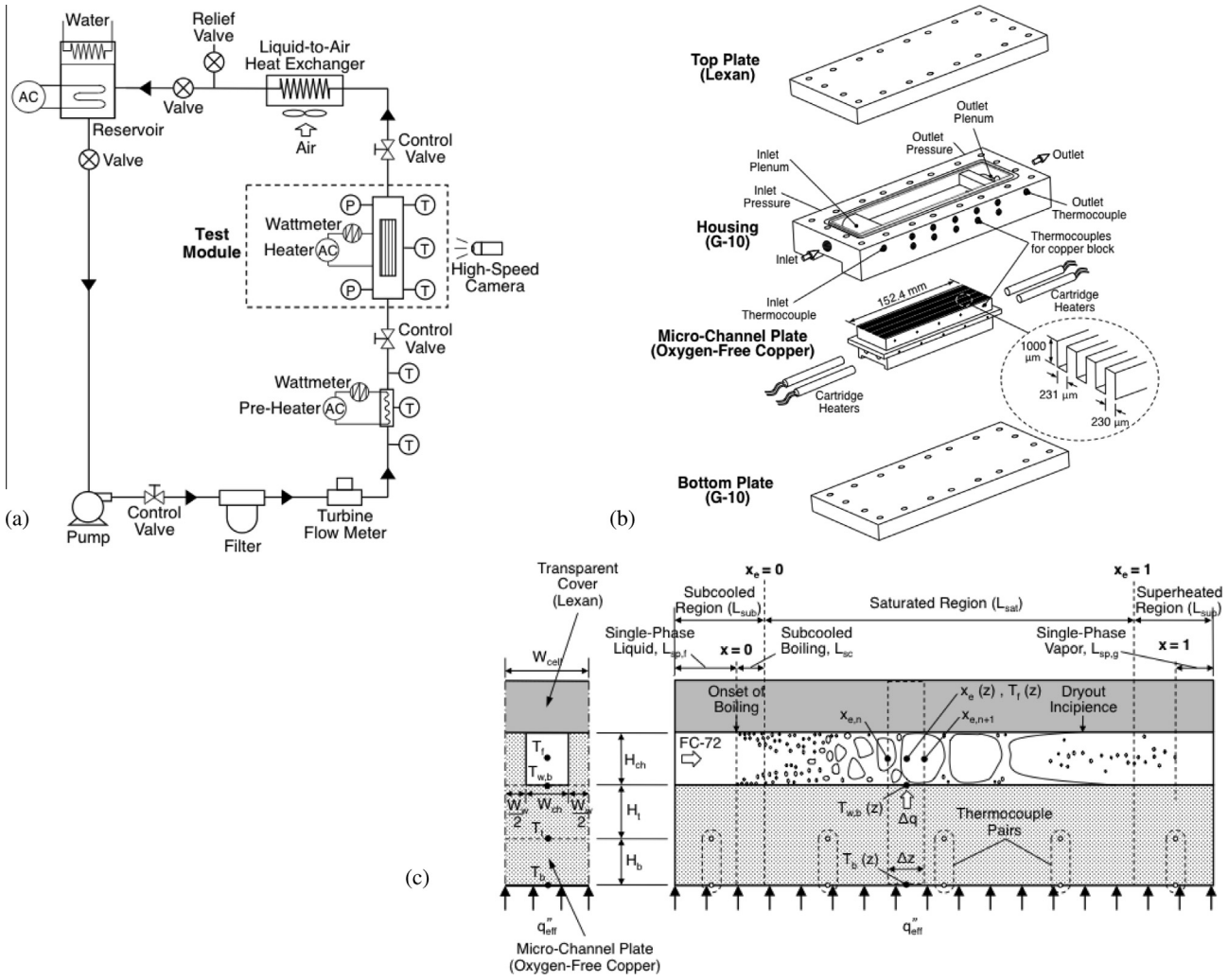

Fig. 1. (a) Schematic of flow loop. (b) Test module construction and instrumentation. (c) Cross- and longitudinal sections of microchannel test module and associated nomenclature and heat transfer regimes.

3. Results and discussion

3.1. Heat transfer results

Fig. 1(c) shows cross- and longitudinal sections of the test module's copper block along with definitions of flow regions along the micro-channel, temperature measurement locations, and geometrical parameters. FC-72 is introduced into the test module in subcooled state and the length of the subcooled region is determined by axial location where $x_e = 0$.

$$L_{sub} = \frac{\dot{m} c_{p,f} (T_{sat,0} - T_{in})}{q''_{eff} (W_{ch} + W_W)}, \quad (1)$$

where $\dot{m}$, $T_{sat,0}$ and q''_{eff} are the mass flow rate per micro-channel, saturation temperature at the axial location where $x_e = 0$, and effective heat flux based on total width of unit cell containing a single micro-channel, respectively. The effective heat flux at each axial location of a thermocouple pair is based on the assumption of one-dimensional heat conduction perpendicular to the direction of fluid flow.

Table 1
Operating conditions of present study.

	Horizontal		Vertical upward		Vertical downward	
	Pressure drop	Heat transfer	Pressure drop	Heat transfer	Pressure drop	Heat transfer
G (kg/m^2 s)	155.9–792.0	196.6–792.0	151.5–834.5	259.2–834.5	175.4–772.3	175.4–772.3
G/ρ_f (m/s)	0.10–0.50	0.13–0.50	0.10–0.53	0.17–0.53	0.11–0.49	0.11–0.49
q''_{eff} (W/cm^2)	2.19–9.46	3.10–9.41	2.14–9.56	3.43–9.56	2.47–9.89	3.28–9.30
P_{in} (kPa)	188.1–297.3	188.1–297.3	187.8–292.2	187.8–292.2	189.3–306.5	189.3–306.5
T_{sat} (°C)	76.5–93.1	76.5–93.1	76.4–92.5	76.4–92.5	76.7–94.3	76.7–94.3
T_{in} (°C)	60.5–83.2	60.5–81.0	60.2–83.3	60.2–81.8	60.8–84.1	60.8–84.1
$x_{e,in}$	−0.29 to −0.09	−0.29 to −0.09	−0.28 to −0.10	−0.28 to −0.11	−0.29 to −0.09	−0.29 to −0.09
P_R	0.09–0.16	0.10–0.16	0.10–0.16	0.10–0.16	0.09–0.17	0.10–0.17
Data points	97	65	80	65	97	86

Table 2
Thermophysical properties of saturated FC-72 at T_{sat} = 78.6 °C (P_{sat} = 2 bar).

ρ_f (kg/m^3)	ρ_g (kg/m^3)	k_f (W/m K)	μ_f (kg/m s)	$c_{p,f}$ (J/kg K)	h_{fg} (kJ/kg)	σ (mN/m)
1,535	25.85	0.0514	349×10^{-6}	1,136	87.27	6.2

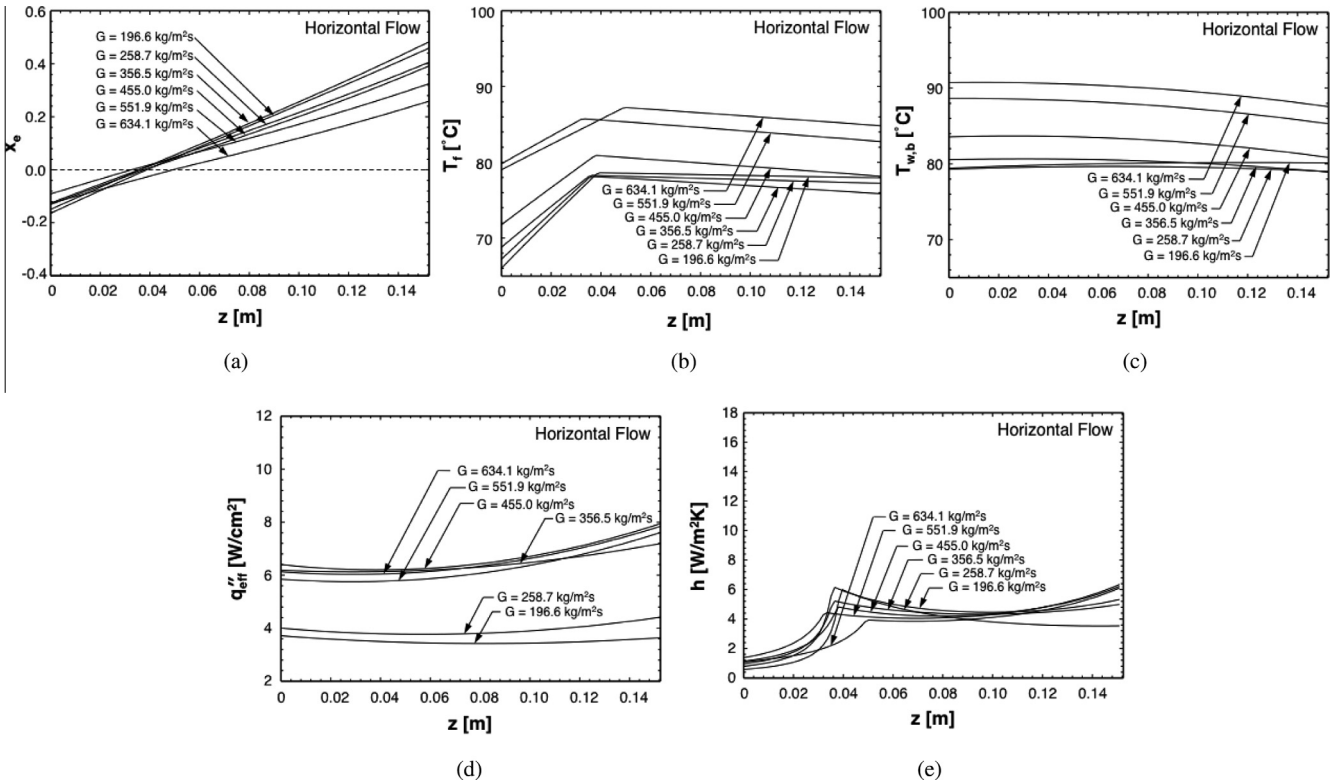

Fig. 2. Axial variations of (a) thermodynamic equilibrium quality, (b) fluid temperature, (c) micro-channel bottom wall temperature, (d) effective heat flux, and (e) heat transfer coefficient for six mass velocities in horizontal flow.

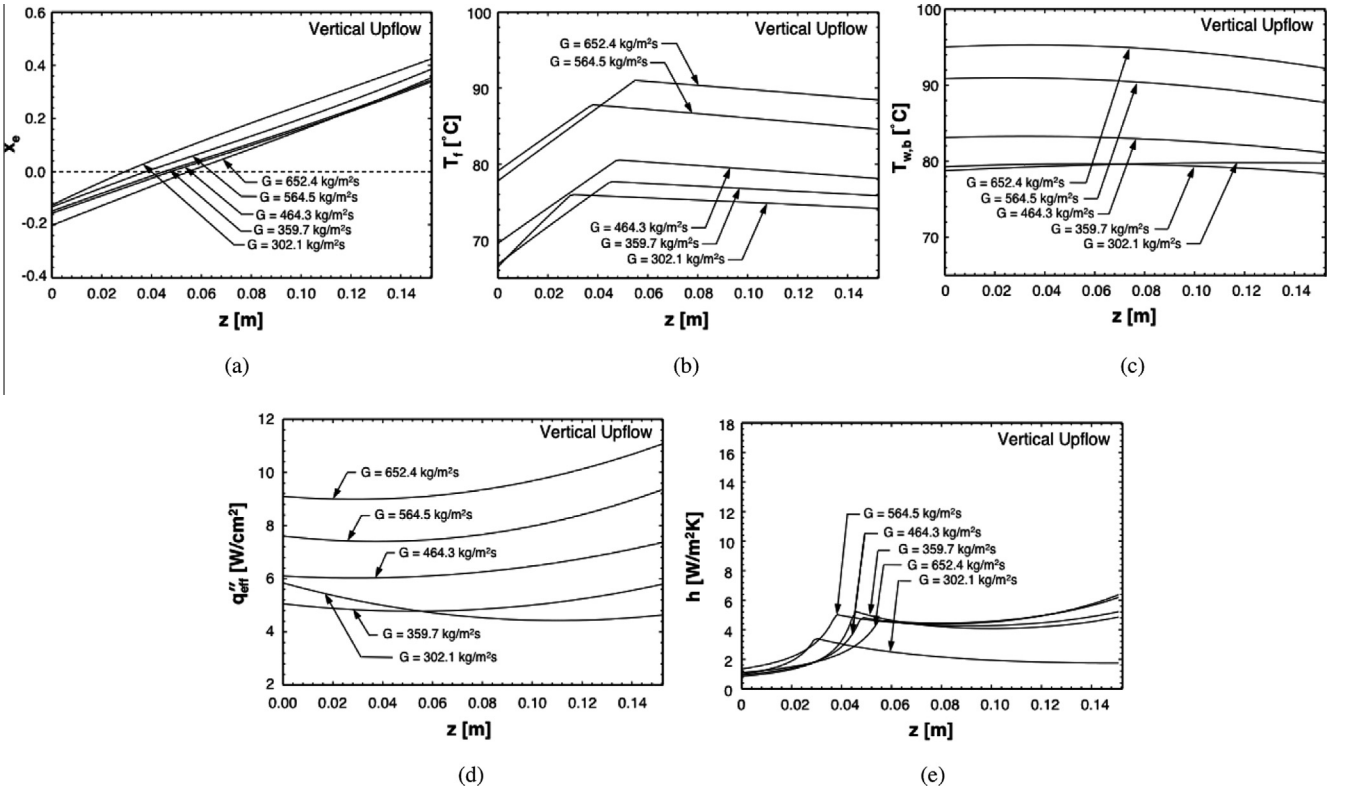

Fig. 3. Axial variations of (a) thermodynamic equilibrium quality, (b) fluid temperature, (c) micro-channel bottom wall temperature, (d) effective heat flux, and (e) heat transfer coefficient for six mass velocities in vertical upflow.

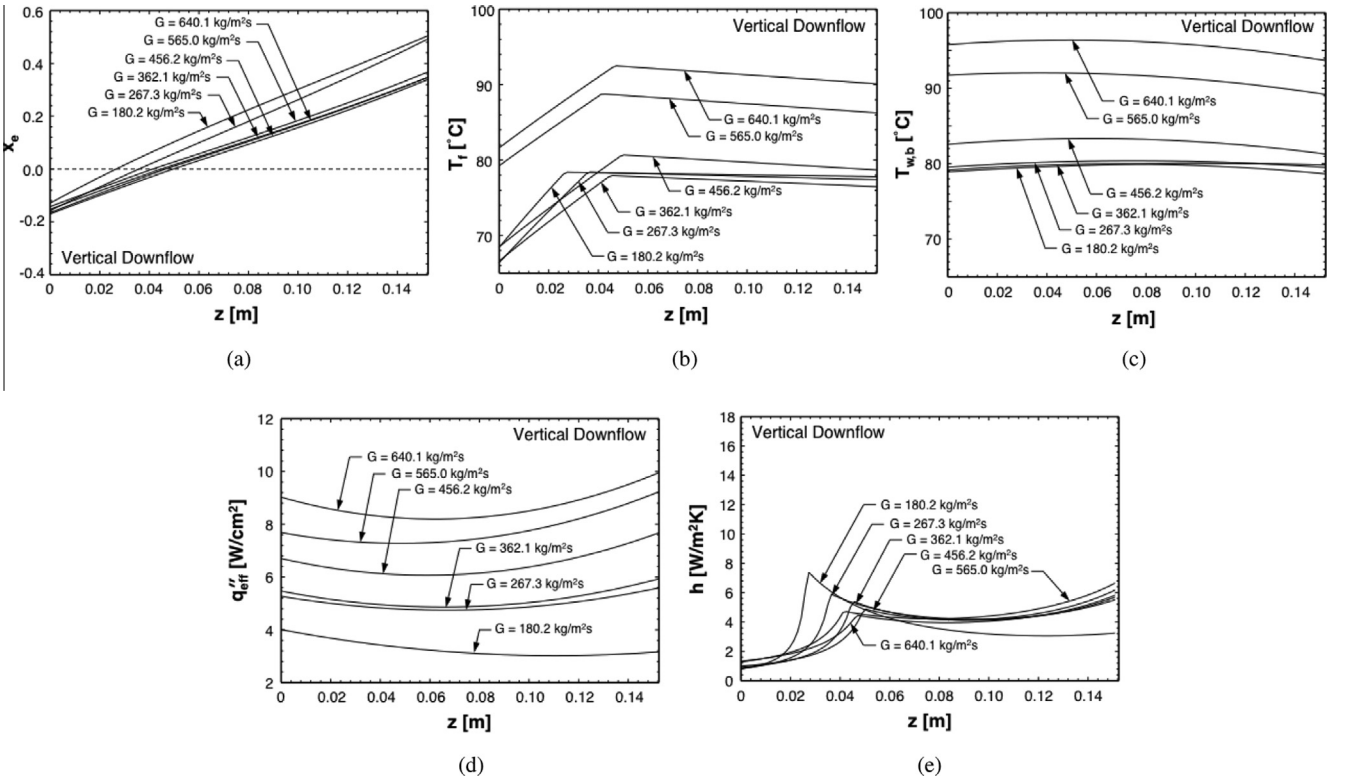

Fig. 4. Axial variations of (a) thermodynamic equilibrium quality, (b) fluid temperature, (c) micro-channel bottom wall temperature, (d) effective heat flux, and (e) heat transfer coefficient for six mass velocities in vertical downflow.

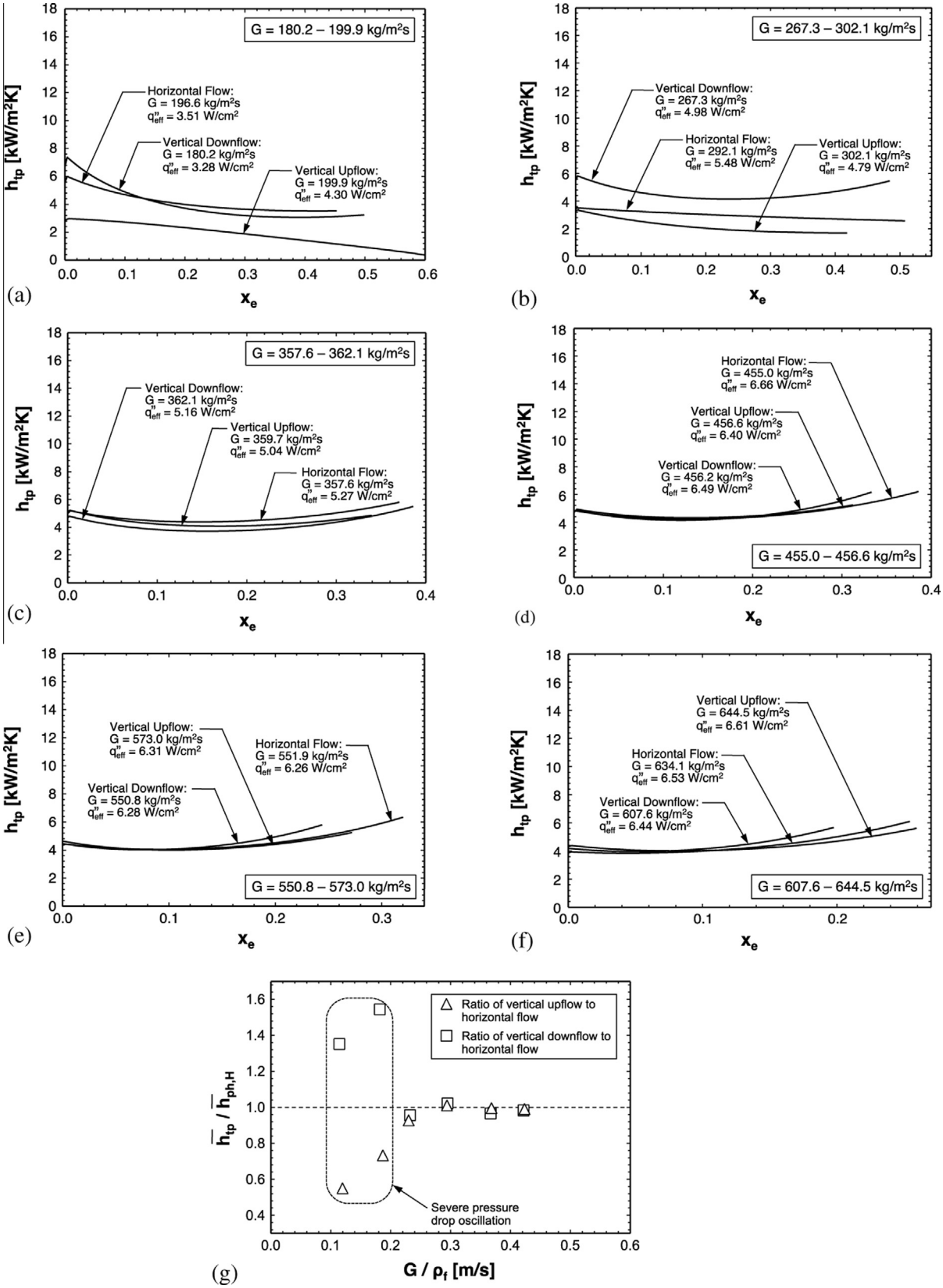

Fig. 5. Variations of experimentally-determined two-phase heat transfer coefficient with thermodynamic equilibrium quality for horizontal flow, vertical upflow and vertical downflow at (a) $G = 180.2–199.9\ kg/m^2\,s$, (b) $G = 267.3–302.1\ kg/m^2\,s$, (c) $G = 357.6–362.1\ kg/m^2\,s$, (d) $G = 455.0–456.6\ kg/m^2\,s$, (e) $G = 550.8–573.0\ kg/m^2\,s$, and (f) $G = 607.6–644.5\ kg/m^2\,s$. (g) Variations of heat transfer coefficient averaged over twophase region with mass velocity; heat transfer coefficients for vertical upflow and vertical downflow are normalized relative to those for horizontal flow.

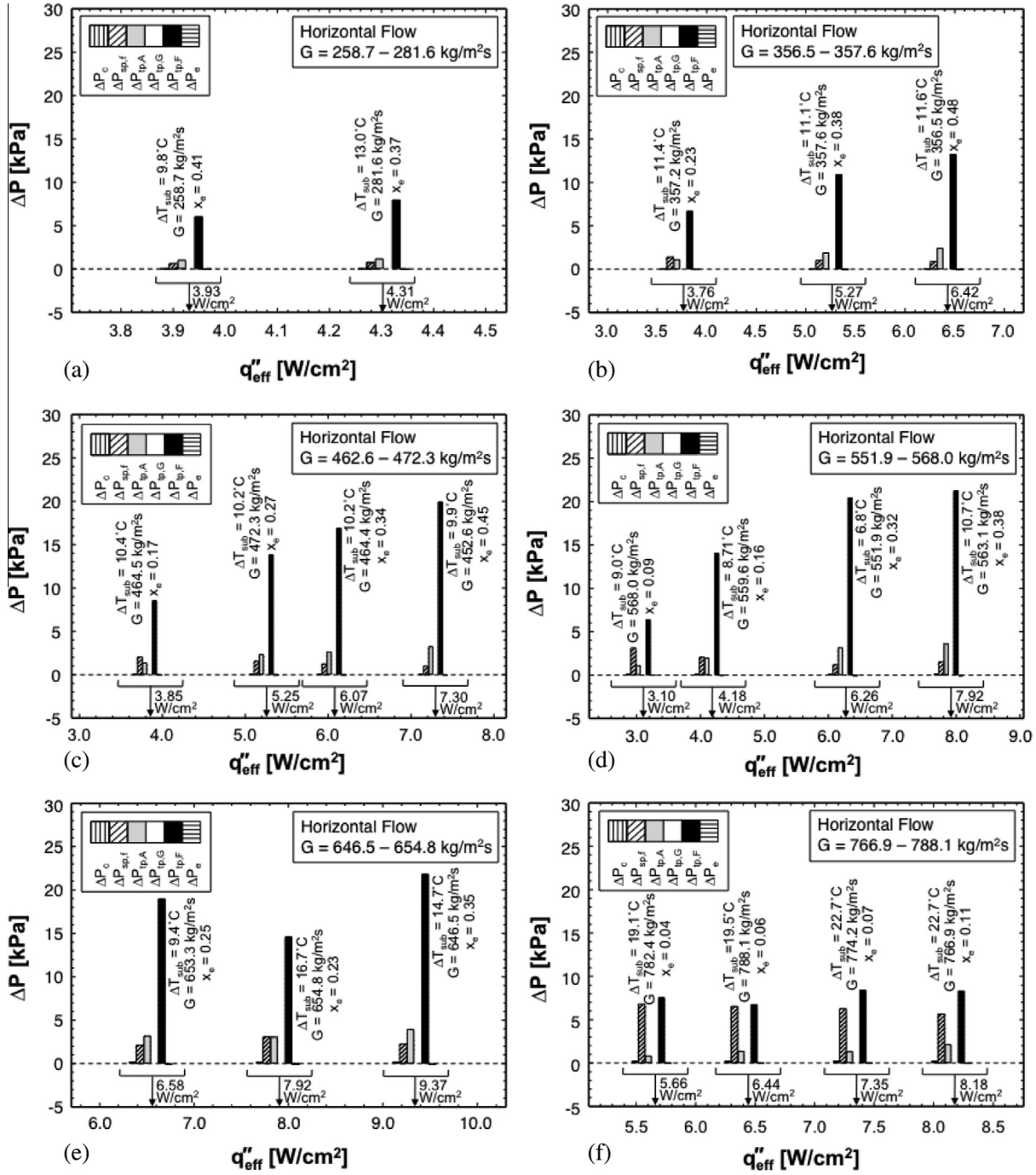

Fig. 6. Variation of pressure drop components with effective heat flux for horizontal flow with (a) $G = 258.7–281.6$ kg/m^2 s, (b) $G = 356.5–357.6$ kg/m^2 s, (c) $G = 462.6–472.3$ kg/m^2 s, (d) $G = 551.9–568.0$ kg/m^2 s, (e) $G = 646.5–654.8$ kg/m^2 s, and (f) $G = 766.9–788.1$ kg/m^2 s.

$$q''_{eff} = k_s \frac{(T_b - T_t)}{H_b}, \tag{2}$$

where T_b and T_t are the lower and upper temperatures of the copper block measured at each of the five axial thermocouple locations.

The local heat transfer coefficient is calculated by applying an energy balance to the unit cell and using the fin analysis method.

$$q''_{eff}(W_{ch} + W_W) = h(T_{w,b} - T_f)(W_{ch} + 2\eta H_{ch}), \tag{3}$$

where η is the fin efficiency for a rectangular fin with an adiabatic tip, which is given by

$$\eta = \frac{tanh(mH_{ch})}{mH_{ch}}, \tag{4}$$

$$\text{where} \quad m = \sqrt{\frac{2h}{k_s W_W}}. \tag{5}$$

Heat loss through the top and the sides of the unit cell are neglected because of the low thermal conductivity of the top cover (0.20 W/m K) and symmetry between adjacent cells, respectively. The temperature $T_{w,b}$ of the micro-channel's bottom wall is calculated using the assumption of one-dimensional heat diffusion,

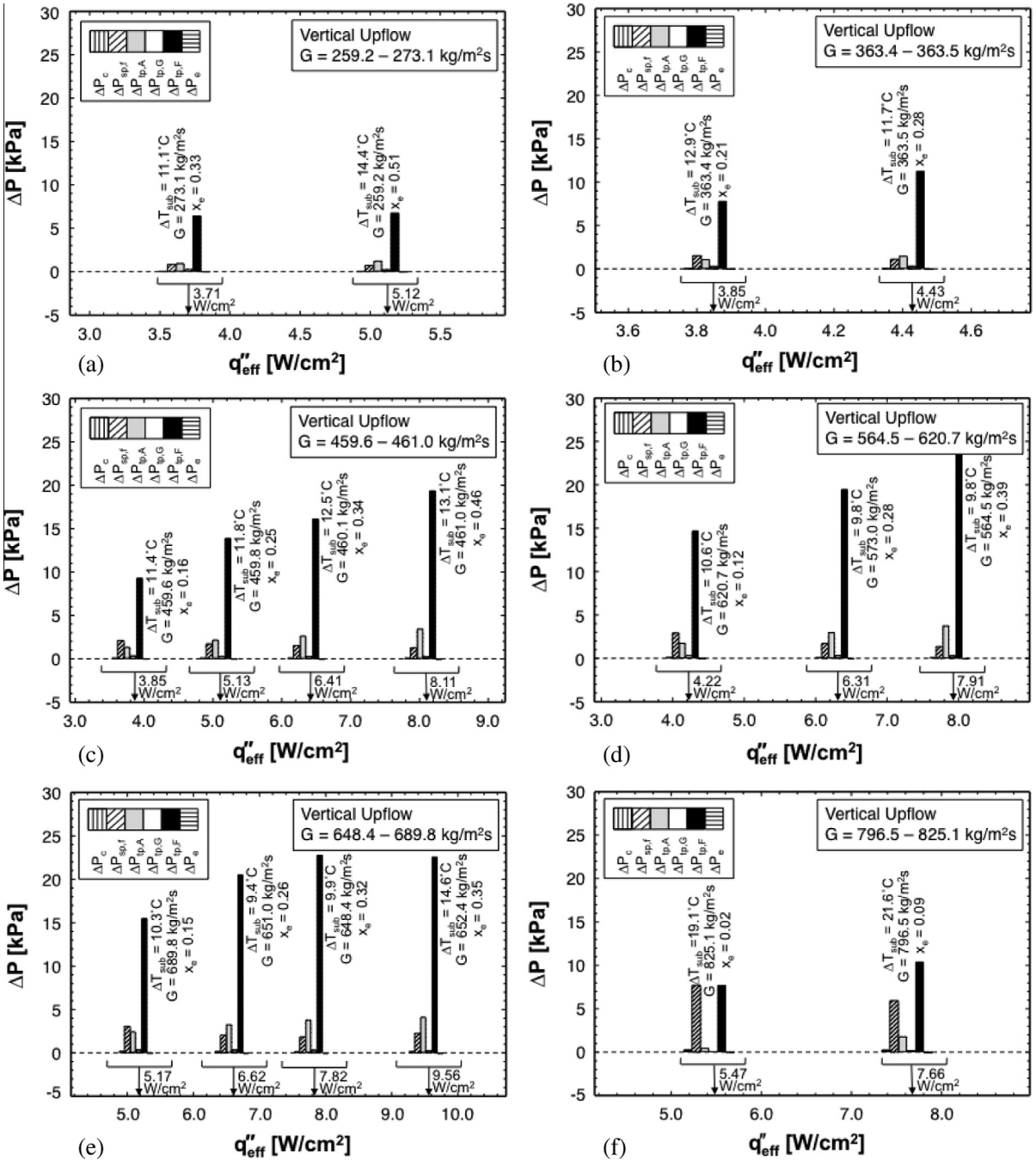

Fig. 7. Variation of pressure drop components with effective heat flux for vertical upflow with (a) $G = 259.2–273.1$ kg/m^2 s, (b) $G = 363.4–363.5$ kg/m^2 s, (c) $G = 459.6–461.0$ kg/m^2 s, (d) $G = 564.5–620.7$ kg/m^2 s, (e) $G = 648.4–689.8$ kg/m^2 s, and (f) $G = 796.5–825.1$ kg/m^2 s.

$$T_{w,b} = T_t - \frac{q''_{eff} H_t}{k_s}. \tag{6}$$

The axial variation of the bulk fluid temperature along the micro-channel is determined as follows:

$$T_{f,n+1} = T_{f,n} + \frac{q''_{eff}(W_{ch} + W_W)\Delta z}{\dot{m} c_{p,f}} \quad \text{for } x_e < 0, \tag{7a}$$

$$T_f = T_{sat} \quad \text{for } 0 \leqslant x_e \leqslant 1, \tag{7b}$$

$$\text{and} \quad T_{f,n+1} = T_{f,n} + \frac{q''_{eff}(W_{ch} + W_W)\Delta z}{\dot{m} c_{p,g}} \quad \text{for } x_e > 1. \tag{7c}$$

The thermodynamic equilibrium quality along the micro-channel is determined from

$$x_e = -\frac{c_{p,f}(T_{sat} - T_f)}{h_{fg}} \quad \text{for } x_e < 0, \tag{8a}$$

$$x_{e,n+1} = x_{e,n} + \frac{q''_{eff}(W_{ch} + W_W)\Delta z}{\dot{m} h_{fg}} \quad \text{for } 0 \leqslant x_e \leqslant 1, \tag{8b}$$

$$\text{and} \quad x_e = 1 + \frac{c_{p,g}(T_f - T_{sat})}{h_{fg}} \quad \text{for } x_e > 1, \tag{8c}$$

where the saturation temperature is determined from the local saturation pressure.

Figs. 2–4 show axial variations of the thermodynamic equilibrium quality, x_e, bulk fluid temperature, T_f, bottom wall temperature, $T_{w,b}$, effective heat flux, q''_{eff}, and heat transfer coefficient, h, for different mass velocities for horizontal flow, vertical upflow

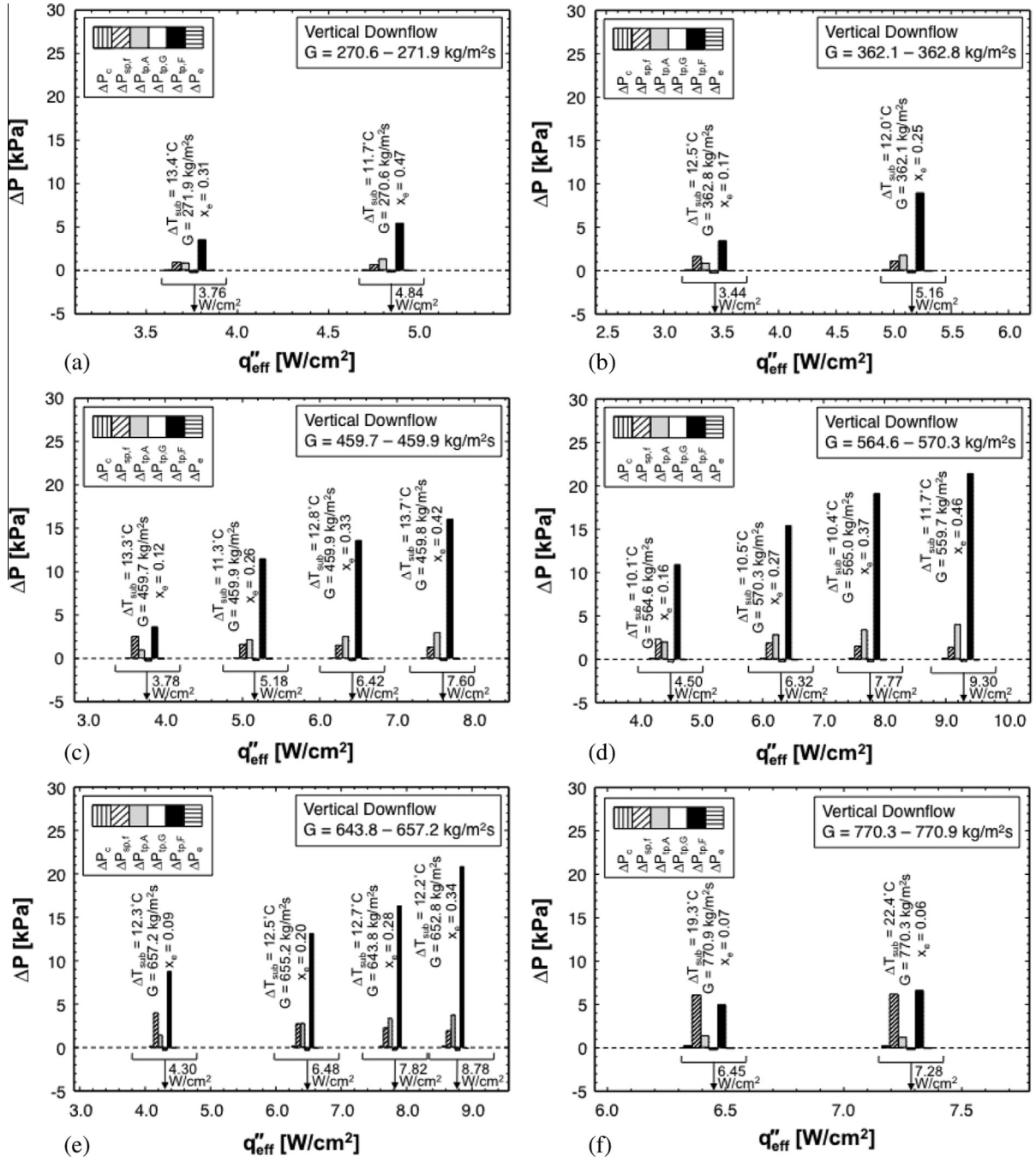

Fig. 8. Variation of pressure drop components with effective heat flux for vertical downflow with (a) $G = 270.6–271.9$ kg/m^2 s, (b) $G = 362.1–362.8$ kg/m^2 s, (c) $G = 459.7–459.9$ kg/m^2 s, (d) $G = 564.6–570.3$ kg/m^2 s, (e) $G = 643.8–657.2$ kg/m^2 s, and (f) $G = 770.3–770.9$ kg/m^2 s.

and vertical downflow, respectively. Since the copper block temperatures are measured by thermocouple pairs at five discrete axial locations, temperatures in between are obtained from second-order polynomial curve-fits to axial distance. The axial variations of q''_{eff} and h are calculated using corresponding copper block temperatures. The bottom micro-channel wall temperature, $T_{w,b}$, and bulk fluid temperature, T_f, are pressure dependent, especially in the two-phase region; both temperatures increase with increasing saturation pressure.

Notice in Figs. 2–4 that x_e increases fairly linearly with z with the slope inversely proportional to G; any nonlinearity is attributed to axial variations in the saturation pressure. All cases include a single-phase liquid region at the inlet where $x_e < 0$. This region is clearly identifiable in the axial variation of T_f in the form of a fairly linear and rather sharp axial increase. Notice that, because of the axially decreasing pressure, T_f is not constant in the two-phase region but decreases slightly since $T_f = T_{sat}$ in this region. The effect of decreasing pressure in the two-phase region is also captured in the axial variation of the bottom wall temperature, $T_{w,b}$. The effective heat flux decreases slightly in the single-phase liquid region because of the decreasing difference between the bottom wall and bulk fluid temperatures. For most cases, the effective heat flux increases monotonically in the saturated region. The magnitude of the local heat transfer coefficient is dictated by local values of q''_{eff} and $T_{w,b} - T_f$. The local heat transfer coefficient increases appreciably in the single-phase liquid region because of the large decrease in $T_{w,b} - T_f$. The heat transfer coefficient is higher in the two-phase region because of both high q''_{eff} and small $T_{w,b} - T_f$.

It has been widely accepted that the saturated flow boiling region is governed by two different mechanisms [45]: nucleate boiling (*nb*) dominated heat transfer and convective boiling (*cb*) dominated heat transfer. The nucleate boiling dominated heat transfer is typically governed by bubbly and slug flow, where the heat transfer coefficient is dependent on heat flux rather than mass velocity or quality. On the other hand, the convective boiling dominated heat transfer is associated mostly with annular flow, where the heat transfer coefficient is far less sensitive to the heat flux. In this study, the working fluid is introduced to the micro-channels in subcooled state and exits as a saturated two-phase mixture, with the flow regime in the saturated region changing from bubbly to annular flow. Therefore, the contributions of nucleate boiling (*nb*) and convective boiling (*cb*) are expected to vary greatly along the channel.

Fig. 5 compares, for six different ranges of mass velocity, the variation of the heat transfer coefficient associated with the two-phase region ($x_e > 0$) for the three flow orientations. There is appreciable variation of h_{tp} with x_e among the three orientations for the two lowest mass velocities, Fig. 5(a) and (b), respectively, and nearly identical variations for the four highest mass velocities, Fig. 5(c)–(f). These results demonstrate the important role of buoyancy force at low mass velocities. However, because of differences in operating pressure among the different orientations, it is not possible to generalize the trend depicted in Fig. 5(a) and (b) of vertical downflow yielding the highest h_{tp}, followed by horizontal flow and vertical upflow. For all three orientations, the pressure at the inlet to the test module is maintained at 2 bar. Because of gravitational effects, the average pressure for the entire channel is therefore higher for vertical downward, followed by horizontal flow, and with vertical upflow yielding the lowest average pressure. Fig. 5(c)–(f) show the heat transfer coefficient in the two-phase region is fairly independent of orientation as buoyancy effects appear to be dwarfed by inertia for $G > 357.6$ kg/m^2 s.

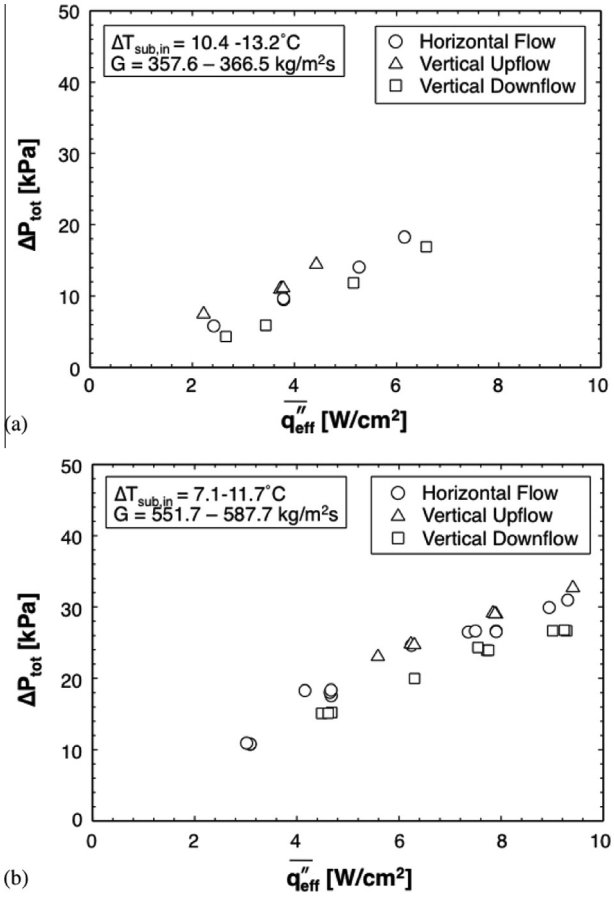

Fig. 9. Variation of measured total pressure drop with average effective heat flux for (a) $G = 357.6$–366.5 kg/m^2 s and (b) $G = 551.7$–587.7 kg/m^2 s.

The effect of G is more clearly illustrated in Fig. 5(g), which shows htp results averaged over the entire channel length as a function of G/ρ_f. The results for vertical upflow and vertical downflow are normalized by those for horizontal flow. Notice the strong departure in the average heat transfer coefficient data for the different orientations at low mass velocities and convergence to an asymptotic value of unity for $G/\rho_f > 0.22$. It should be noted that the data corresponding to the two lowest mass velocities in Fig. 5(g) are measured during *severe pressure drop oscillation* as discussed in the next section.

3.2. Pressure drop results

Total pressure drop across the micro-channels is the difference between pressures measured by the pressure transducers in the inlet and outlet plenums. The total pressure is the sum of as many as five components: inlet contraction, ΔP_c, single-phase liquid region, $\Delta P_{sp,f}$, two-phase region, ΔP_{tp}, single-phase vapor region, $\Delta P_{sp,g}$, and outlet expansion, ΔP_e,

$$\Delta P_{tot} = \Delta P_c + \Delta P_{sp,f} + \Delta P_{tp} + \Delta P_{sp,g} + \Delta P_e. \tag{9}$$

The inlet contraction and outlet expansion components can be determined from [46]

$$\Delta P_c = \frac{G^2 v_f}{2}\left[\left(\frac{1}{C_c} - 1\right)^2 + (1 - \sigma_c^2)\right]\left[1 + \frac{v_{fg} x_{e,in}}{v_f}\right] \tag{10}$$

$$\text{and} \quad \Delta P_e = G^2 \sigma_c (\sigma_c - 1) v_f \left[1 + \frac{v_{fg} x_{e,out}}{v_f}\right], \tag{11}$$

$$\text{where} \quad \sigma_c = \frac{W_{ch} H_{ch} N_{ch}}{W_p H_p}. \tag{12}$$

Geiger [47] proposed a relation for the contraction coefficient, C_c, for single-phase liquid flow in the inlet plenum which he expressed as a function of contraction ratio, σ_c,

$$C_c = 1 - \frac{1 - \sigma_c}{2.08(1 - \sigma_c) + 0.5371}. \tag{13}$$

Pressure drop for the upstream single-phase liquid region and downstream vapor region can be determined from [46]

$$\Delta P_{sp,k} = \frac{2 L_{sp,k}}{D_h} f_{sp,k} G^2 v_k, \tag{14}$$

where subscript k refers to either liquid, f, or vapor, g, and $f_{sp,k}$ is the Fanning friction factor, which is obtained from [46,48,49]

$$f_{sp,k}\mathrm{Re}_k = 24[1 - 1.3553\beta + 1.9467\beta^2 - 1.7012\beta^3 + 0.9564\beta^4 - 0.2537\beta^5] \quad \text{for } \mathrm{Re}_k < 2000, \tag{15a}$$

$$f_{sp,k} = 0.079\mathrm{Re}_k^{-0.25} \quad \text{for } 2000 < \mathrm{Re}_k < 20{,}000, \tag{15b}$$

$$\text{and} \quad f_{sp,k} = 0.046\mathrm{Re}_k^{-0.2} \quad \text{for } 20{,}000 < \mathrm{Re}_k. \tag{15c}$$

It is assumed that transition from single-phase liquid flow to two-phase flow occurs at $x_e = 0$ and the single-phase liquid flow is fully-developed, and Reynolds number in Eqs. (15a)–(15c) is defined as

$$\mathrm{Re}_k = \frac{G D_h}{\mu_k}. \tag{16}$$

Pressure drop for the two-phase region consists of three separate components: accelerational, gravitational, and frictional,

$$\Delta P_{tp} = \Delta P_{tp,A} + \Delta P_{tp,G} + \Delta P_{tp,F} = \int_0^{L_{tp}} \left[-\left(\frac{dP}{dz}\right)_{tp,A} - \left(\frac{dP}{dz}\right)_{tp,G} - \left(\frac{dP}{dz}\right)_{tp,F} \right] dz. \quad (17)$$

For steady flow in a channel with a constant flow area, the accelerational, gravitational and frictional pressure gradients are expressed, respectively, as

$$-\left(\frac{dP}{dz}\right)_{tp,A} = G^2 \frac{d}{dz}\left[\frac{x_e^2 v_g}{\alpha} + \frac{(1-x_e)^2 v_f}{1-\alpha}\right], \quad (18)$$

$$-\left(\frac{dP}{dz}\right)_{tp,G} = \bar{\rho} g \sin\theta = \left[\frac{\alpha}{v_g} + \frac{(1-\alpha)}{v_f}\right] g \sin\theta, \quad (19)$$

and $$-\left(\frac{dP}{dz}\right)_{tp,F} = \frac{2}{D_h} f_{tp} G^2 v_f \left(1 + x_e \frac{v_{fg}}{v_f}\right), \quad (20)$$

where f_{tp} is the two-phase Fanning friction factor, which will be discussed in the second part of this study [44] in conjunction with the Homogeneous Equilibrium Model (HEM) and Separated Flow Model (SFM).

HEM is the simplest method for determining void fraction, α, that appears in both the accelerational and gravitational pressure gradients, Eqs. (18) and (19), respectively. The HEM employs the relation $\bar{\rho} = 1/\bar{v}$ to obtain

$$\bar{\rho} = \left[\frac{\alpha}{v_g} + \frac{(1-\alpha)}{v_f}\right] = \frac{1}{x_e v_g + (1-x_e) v_f} = \frac{1}{\bar{v}}, \quad (21)$$

which yields $$\alpha = \left[1 + \left(\frac{1-x_e}{x_e}\right)\left(\frac{v_f}{v_g}\right)\right]^{-1}. \quad (22)$$

To assess the relative importance of individual pressure drop components to total pressure drop for different mass velocities and different orientations, a simple approach is adopted in which Eq. (22), which is derived using the HEM, is used to determine both the accelerational and gravitational pressure drops. All liquid and vapor properties in the two-phase region are based on local saturation pressure. Pressure drops associated with inlet contraction and outlet expansion are determined from Eqs. (10) and (11), respectively, and pressure drop for the single-phase liquid region from Eq. (14). The downstream single-phase vapor region is never encountered since exit quality is maintained below unity to preclude CHF occurrence. Since the total pressure drop is measured experimentally between the inlet and outlet plenums of the test module, Eq. (9) and (17) can be used to calculate the frictional pressure drop. This method avoids reliance on any models or correlations to determine $\Delta P_{tp,F}$. Details concerning the prediction of the frictional pressure drop are deferred to the second part of this study [44].

Figs. 6–8 show variations of the individual pressure drop components with q''_{eff} and G for horizontal flow, vertical upward and vertical downflow, respectively. Excepting a few cases, total pressure drop for the different orientations and mass velocities increases with increasing q''_{eff}. Notice that pressure drop for most cases is largely dominated by two-phase friction followed, to a lesser degree, by two-phase acceleration and single-phase liquid friction, with the contraction and expansion providing negligible contributions.

The frictional pressure drop increases with increasing q''_{eff} for constant G because of the combined effects of increased length of the two-phase region and larger vapor quality. The accelerational

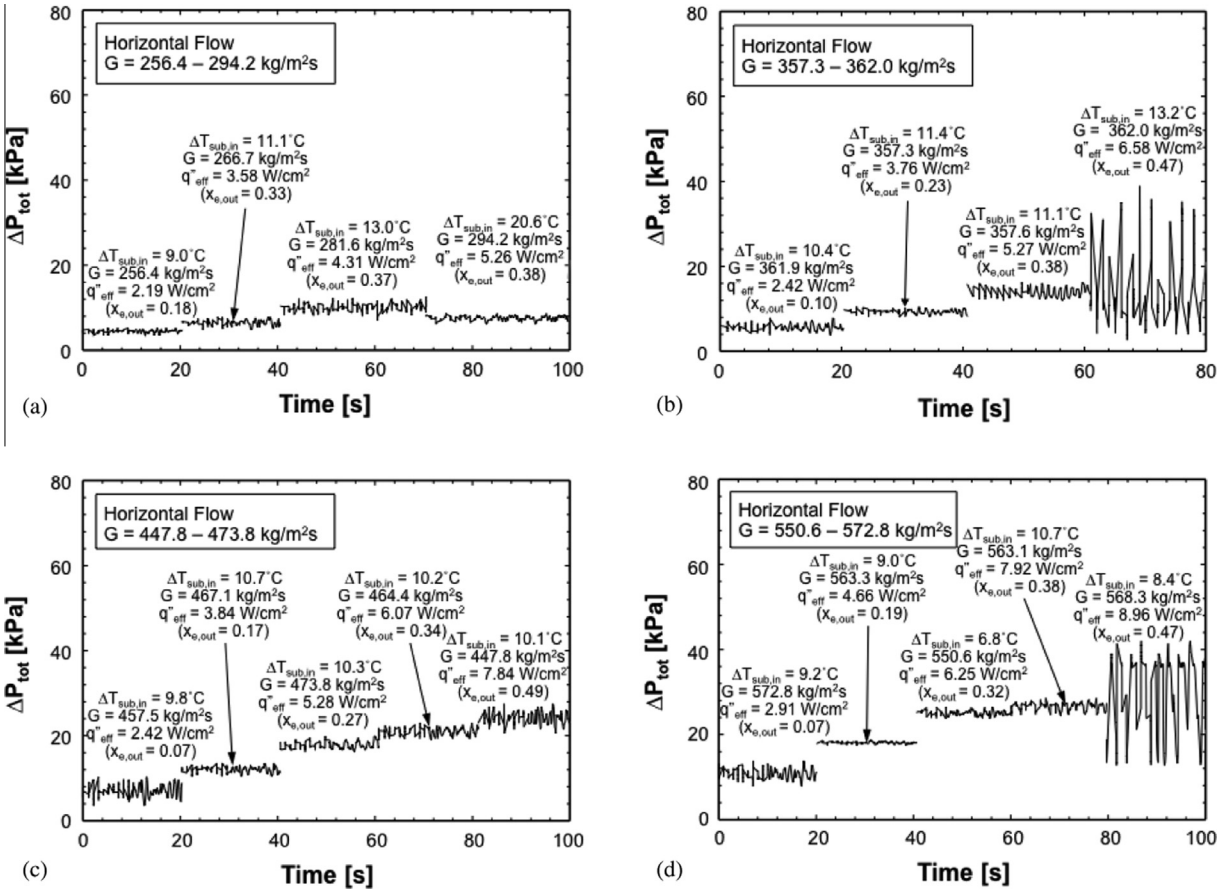

Fig. 10. Temporal variations of total pressure drop across test section in horizontal flow with (a) G = 256.4–294.2 kg/m^2 s, (b) G = 357.3–362.0 kg/m^2 s, (c) G = 447.8–473.8 kg/m^2 s, and (d) G = 550.6–572.8 kg/m^2 s.

pressure drop also increases with increasing q''_{eff} for constant G because of increased flow velocity brought about by the increased vapor quality. The single-phase liquid pressure drop for all three orientations increases mostly with increasing G.

Notice that the gravitation pressure drop is zero for horizontal flow, Fig. 6, positive for vertical upflow, Fig. 7, and negative for vertical downflow, Fig. 8. The magnitude of the gravitational pressure drop for vertical upflow and downflow decreases with increasing q''_{eff} as increased vapor production decreases the density of the two-phase mixture. However, Figs. 7 and 8 show that the gravitational pressure drops for vertical upflow and vertical downflow, respectively, are miniscule compared to two-phase friction and acceleration and single-phase liquid friction.

Fig. 9(a) and (b) show the variation of total pressure drop for the three orientations with heat flux for G = 357.6–366.5 and 551.7–587.7 kg/m^{2}s, respectively, where heat flux is averaged over the entire micro-channel length. For each mass velocity range, the total pressure drop increases monotonically with increasing heat flux for all three orientations. This is mostly the result of increased two-phase frictional and acceleration pressure drops as discussed in conjunction with Figs. 6–8.

3.3. Flow instabilities

As discussed in [45,50], flow instabilities are a prime concern for two-phase flow in micro-channel heat sinks. The present study confirms the occurrence of these anomalies, which are captured in Figs. 10–12 as temporal records of total pressure drop measured between the inlet and the outlet of the test module for horizontal flow, vertical upflow and vertical downflow, respectively. For each orientation, these records are captured for each of four narrow ranges of mass velocity in response to increasing heat flux. Like [45], two main types of instability are encountered and confirmed by video, *mild parallel channel instability* and *severe pressure drop oscillations*.

As shown in Figs. 10–12, the mild parallel channel instability is observed in all three orientations at relatively low and moderate heat fluxes. This type of instability is triggered by differences in boiling behavior between parallel micro-channels as well as non-uniform flow rate distribution between channels. For the same heat flux, a channel with a smaller flow rate produces more vapor than one with a higher flow rate. The low flow rate channel with the higher vapor generation incurs increased flow resistance because of increases in the two-phase frictional and accelerational pressure drops, which causes a reduction in flow rate into the channel. A localized increase in inlet plenum pressure is now able to overcome the increased flow resistance, which increases the flow rate in the previously low flow rate channel. The mild parallel channel instability is observed in a couple of channels having the smallest flow rates under relatively low and moderate heat fluxes.

However, for most cases, further increases in the heat flux trigger severe pressure drop oscillation. This instability is evident in the pressure drop results for horizontal flow, Fig. 10, corresponding to the highest heat flux for three of the four mass velocities. It is also prevalent for vertical upflow, Fig. 11, for the highest heat flux with all four mass velocities, and for vertical downflow, Fig. 12, with only one of the four mass velocities. The severe pressure drop oscillation can be described as follows. High heat fluxes result in high vapor production extending from upstream to downstream in all the channels, resulting in a sudden increase in inlet plenum pressure. The pressure increase eventually increases the flow rate through all the channels, momentarily purging most of the vapor

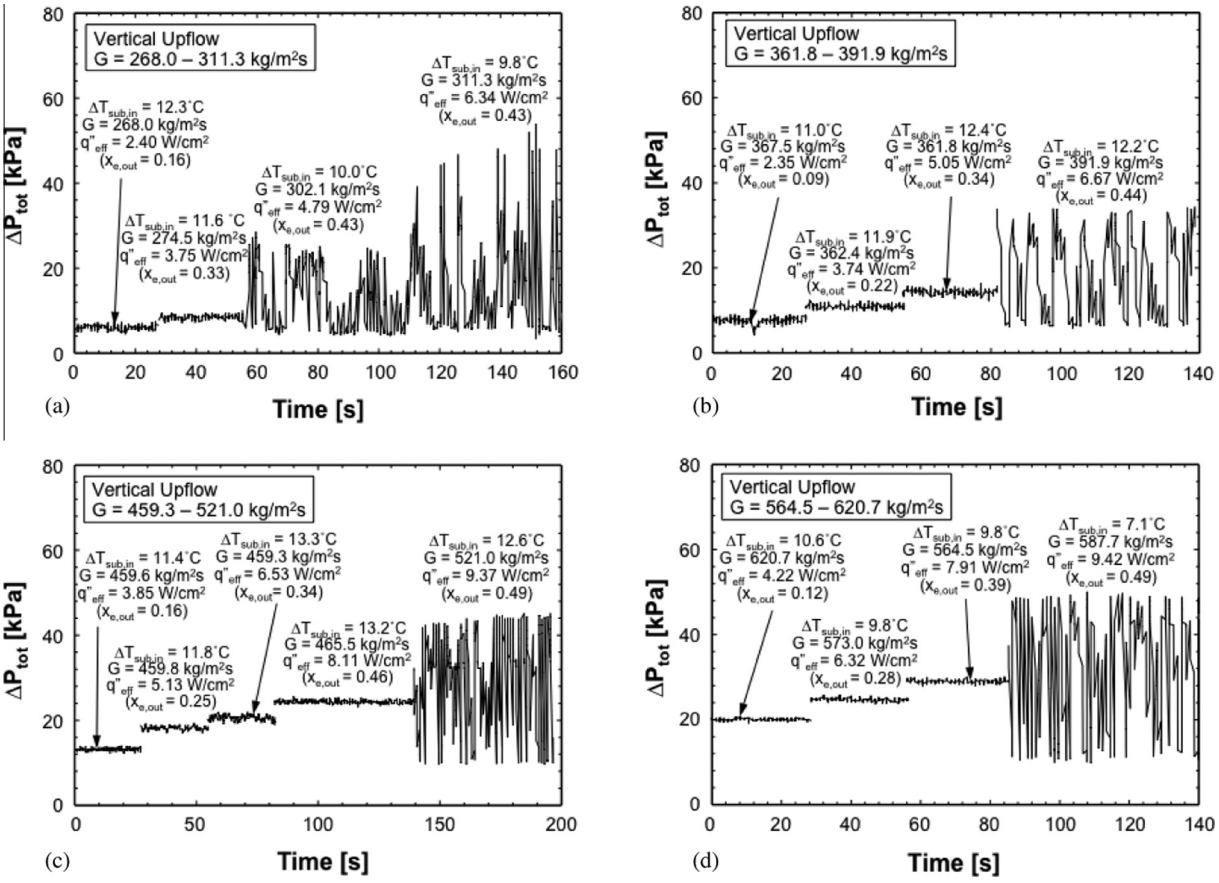

Fig. 11. Temporal variations of total pressure drop across test section in vertical upflow with (a) G = 268.0–311.3 kg/m^2 s, (b) G = 361.8–391.9 kg/m^2 s, (c) G = 459.3–521.0 kg/m^2 s, and (d) G = 564.5–620.7 kg/m^2 s.

from the channels. With the now decreased flow resistance, the inlet pressure decreases. This causes the flow rate to decrease once again and vapor production to increase, initiating a new cycle of instability. Unlike the rather chaotic fluctuations and different flow patterns between channels under the mild parallel channel instability, the fluctuations associated with the severe pressure drop oscillation occur in unison in all channels and with a fairly constant frequency. Furthermore, the pressure drop fluctuations with the severe pressure drop oscillation possess much greater amplitude but lower frequency. Notice in Figs. 10–12 that this amplitude is as high as 50 kPa.

Orientation appears to influence flow instabilities in different ways. Because of the aforementioned higher average pressure in vertical downflow compared to the other two orientations, this orientation provides the most flow stiffness and therefore highest resistance to instability [33]. The opposite is true for vertical upflow, which, for the same test module's inlet conditions as horizontal flow and vertical downflow, suffers the most pronounced instabilities, especially at low mass velocities. It should be emphasized that further decreases of mass velocity for vertical downflow below the test conditions of the present study can be very problematic as buoyancy will begin to exceed the drag forces exerted by liquid on the vapor bubbles, resulting in backflow along the channels [23,33].

It should be noted that the severe pressure drop oscillation has a detrimental effect on the heat transfer coefficient, which is attributed to the expanding vapor volume within the channels during this instability increasing the average wall temperature. The measured reduction in the heat transfer coefficient is as high as 30% compared to flow without instability.

3.4. Flow visualization results

Using high-speed video imaging, flow visualization experiments are conducted at four axial locations of $z = 19.8$, 59.4, 96.0 and 129.5 mm, six FC-72 mass velocities and all three orientations to determine dominant flow regimes.

A key challenge is assigning flow regimes is the need to characterize local conditions relative to flow quality, x, instead of thermodynamic quality, x_e. The latter quality is used in two-phase flow models because it is easily determined from conservation of mass and energy using Eqs. (8a)–(8c). On the other hand, flow quality x, which is a true measure of vapor mass content, is both different from x_e and its magnitude far more difficult to ascertain. Differences between the two are related to local nonequilibrium effects starting in the subcooled boiling region as depicted in Fig. 1(c).

In the present study, x is calculated from x_e using the following expression by Levy [51],

$$x(z) = x_e(z) - x_d(z)\exp\left\{\frac{x_e(z)}{x_d(z)} - 1\right\}, \tag{23}$$

Table 3
Ranges of flow quality, x, for different two-phase flow regimes.

	Bubbly	Slug	Churn	Annular
Horizontal flow	0.0–0.013	0.002–0.073	0.046–0.124	0.127–0.324
Vertical upflow	0.001–0.05	0.003–0.062	0.050–0.138	0.093–0.362
Vertical downflow	0.001–0.002	0.003–0.056	0.040–0.128	0.125–0.393

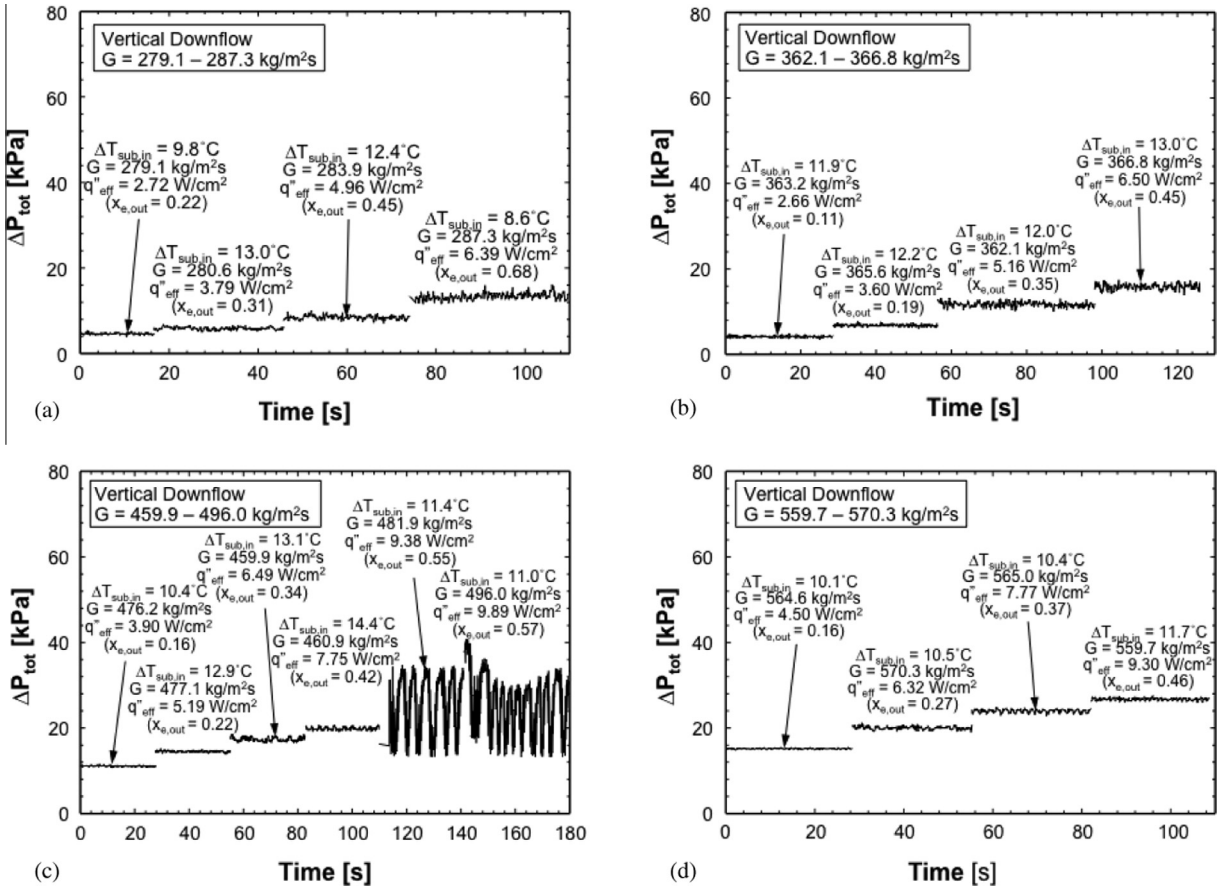

Fig. 12. Temporal variations of total pressure drop across test section in vertical downflow with (a) $G = 279.1$–287.3 kg/m^2 s, (b) $G = 362.1$–366.8 kg/m^2 s, (c) $G = 459.9$–496.0 kg/m^2 s, and (d) $G = 559.7$–570.3 kg/m^2 s.

where x_d (z) is the value of x_e at the point of bubble detachment, which is negative and given by

$$x_d(z) = -\left[\frac{c_{p,f}\Delta T_d(z)}{h_{fg}}\right], \tag{24}$$

$$\text{where} \quad \Delta T_d(z) = q''_H(z)\left[\frac{1}{h_{fo}} - \frac{T_B^+}{\rho_f c_{p,f} u^*}\right], \tag{25}$$

$$T_B^+ = Pr_f Y_B^+ \quad \text{for } 0 \leqslant Y_B^+ \leqslant 5, \tag{26a}$$

$$T_B^+ = 5\left[Pr_f + \ln\left\{1 + Pr_f\left(\frac{Y_B^+}{5} - 1\right)\right\}\right] \quad \text{for } 5 \leqslant Y_B^+ \leqslant 30, \tag{26b}$$

$$T_B^+ = 5\left[Pr_f + \ln(1 + 5Pr_f) + 0.5\ln\left(\frac{Y_B^+}{5}\right)\right] \quad \text{for } 30 \leq Y_B^+. \tag{26c}$$

q''_H, Y_B^+ and u^* in the above relations are the heat flux based on heated perimeter of the channel, nondimensional distance to the tip of the vapor bubble, and friction velocity; the latter two are given, respectively, by

$$Y_B^+ = Y_B\sqrt{\frac{\tau_w}{\rho_f}\frac{\rho_f}{\mu_f}} = 0.015\left(\frac{\sigma D_h}{\tau_w}\right)^{0.5}\sqrt{\frac{\tau_w}{\rho_f}\frac{\rho_f}{\mu_f}} = 0.015\frac{(\rho_f \sigma D_h)^{0.5}}{\mu_f} \tag{27}$$

$$\text{and} \quad u^* = \sqrt{\frac{\tau_w}{\rho_f}} = \sqrt{\frac{f_{fo}}{2}}\frac{G}{\rho_f} \tag{28}$$

and f_{fo} is the Fanning friction factor obtained from Eqs. (15a)–(15c) and (16) for $k = f$ and $sp = fo$ using the liquid-only Reynolds number, Re_{fo}.

Table 3 shows the ranges of flow quality, x, for the different two-phase flow regimes in the three orientations. Notice that, for each orientation, the ranges for different flow regimes overlap depending on local operating conditions.

Most conventional two-phase flow regimes are observed along the micro-channels in the present study as depicted in Fig. 13(a). Table 4 shows the two-phase flow regimes observed at different orientations for different mass velocities and flow qualities. In the low flow quality region, a *bubbly flow regime* is established, where discrete vapor bubbles are generated in a liquid continuum. The bubbles grow along the channels due to the combined effects of evaporation at the bubble interface and coalescence with adjacent bubbles. Once the bubble diameter approaches the width of the channel, the bubbles grow mostly in the longitudinal direction, signaling a transition to the *slug flow regime*. Because of the small aspect ratio of the channel ($\beta = 0.23$), the *slug flow regime* is encountered at very low qualities in the range of $x = 0.002$–0.073. A further increase in quality triggers a transition to the *churn flow regime* as long slug flow vapor bubbles begin to break up, and the flow turns more chaotic and oscillatory. With further increases in quality, the *annular flow regime* is formed as vapor bubbles coalesce axially, forming a continuous vapor core, while the liquid is pushed towards the channel walls in the form of a thin film. Annular flow is fairly dominant in micro-channels where small hydraulic diameter promotes early coalescence of bubbles into a continuous vapor core. The thin annular liquid film is responsible for achieving high heat transfer coefficients in this regime. Two other important influences are turbulence and waviness in the liquid film [52].

The present flow regime data for horizontal flow are compared in Fig. 13(b) to the regime map of Mandhane et al. [53], which is intended for horizontal air–water flows with $D_h = 12.7$–165.1 mm. It is important to note that the parameters used in this comparison are based on x and not x_e. The Mandhane et al. map utilizes superficial liquid velocity, j_f, and superficial vapor velocity, j_g, to distinguish flow regimes. Their map was modified by Dobson and Chato [54] for refrigerant flows by replacing j_g by a modified superficial vapor velocity, which is defined as

$$j'_g = j_g\sqrt{\frac{\rho_g}{\rho_{air}}} \tag{29}$$

to account for the large vapor density differences between air and refrigerants. Fig. 13(b) shows fair agreement with the present horizontal flow data. The map appears very accurate in capturing the boundary for annular flow. However, some of the slug flow data are shifted into the map's bubbly flow region, which may be attributed to the low aspect ratio ($\beta = 0.23$) of the channel used in the present study.

A fundamental weakness of the Mandhane et al. map is the lack of reliance on dimensional parameters to account for different working fluids, flow conditions and channel geometries. Soliman [55] derived a dimensionless approach to predicting transition between mist and annular flows for condensation in tubes. This approach is based on the relationship between modified Weber number, We^*, and Lockhart–Martinelli parameter, X_{tt}, to construct a balance between the destructive and stabilizing forces acting on

Table 4
Flow regimes observed at different orientations for different mass velocities and flow qualities.

	$z = 19.8$ mm	$z = 59.4$ mm	$z = 96.0$ mm	$z = 129.5$ mm
Horizontal flow				
$G = 253.1$ kg/m^2 s	$x = 0.01$: slug	$x = 0.07$: slug	$x = 0.21$: annular	$x = 0.32$: annular
$G = 350.0$ kg/m^2 s	$x = 0.01$: slug	$x = 0.06$: slug	$x = 0.15$: annular	$x = 0.30$: annular
$G = 464.6$ kg/m^2 s	$x = 0.002$: bubbly	$x = 0.03$: slug	$x = 0.08$: churn	$x = 0.12$: churn
$G = 561.9$ kg/m^2 s	$x = 0.00$: bubbly	$x = 0.03$: slug	$x = 0.09$: churn	$x = 0.15$: annular
$G = 643.7$ kg/m^2 s	$x = 0.001$: bubbly	$x = 0.05$: churn	$x = 0.12$: churn	$x = 0.19$: annular
$G = 772.15$ kg/m^2 s	$x = 0.00$: liquid	$x = 0.009$: bubbly	$x = 0.01$: slug	$x = 0.07$: churn
Vertical upward				
$G = 275.3$ kg/m^2 s	$x = 0.006$: slug	$x = 0.06$: slug	$x = 0.14$: churn	$x = 0.26$: annular
$G = 362.9$ kg/m^2 s	$x = 0.004$: slug	$x = 0.06$: churn	$x = 0.17$: annular	$x = 0.27$: annular
$G = 461.0$ kg/m^2 s	$x = 0.002$: bubbly	$x = 0.02$: slug	$x = 0.07$: churn	$x = 0.13$: churn
$G = 625.1$ kg/m^2 s	$x = 0.005$: bubbly	$x = 0.009$: slug		$x = 0.10$: churn
$G = 645.9$ kg/m^2 s	$x = 0.004$: slug	$x = 0.05$: churn	$x = 0.13$: annular	$x = 0.20$: annular
$G = 792.0$ kg/m^2 s	$x = 0.00$: liquid	$x = 0.01$: slug	$x = 0.02$: slug	$x = 0.06$: churn
Vertical downward				
$G = 272.7$ kg/m^2 s	$x = 0.01$: slug	$x = 0.06$: slug	$x = 0.17$: annular	$x = 0.24$: annular
$G = 360.0$ kg/m^2 s	$x = 0.01$: slug	$x = 0.08$: churn	$x = 0.17$: annular	
$G = 464.3$ kg/m^2 s	$x = 0.002$: bubbly	$x = 0.02$: slug	$x = 0.06$: churn	$x = 0.12$: churn
$G = 568.8$ kg/m^2 s	$x = 0.001$: bubbly	$x = 0.02$: slug	$x = 0.07$: churn	$x = 0.13$: churn
$G = 636.0$ kg/m^2 s	$x = 0.001$: bubbly	$x = 0.04$: churn	$x = 0.11$: churn	$x = 0.19$: annular
$G = 761.6$ kg/m^2 s	$x = 0.00$: liquid	$x = 0.02$: slug		$x = 0.05$: churn

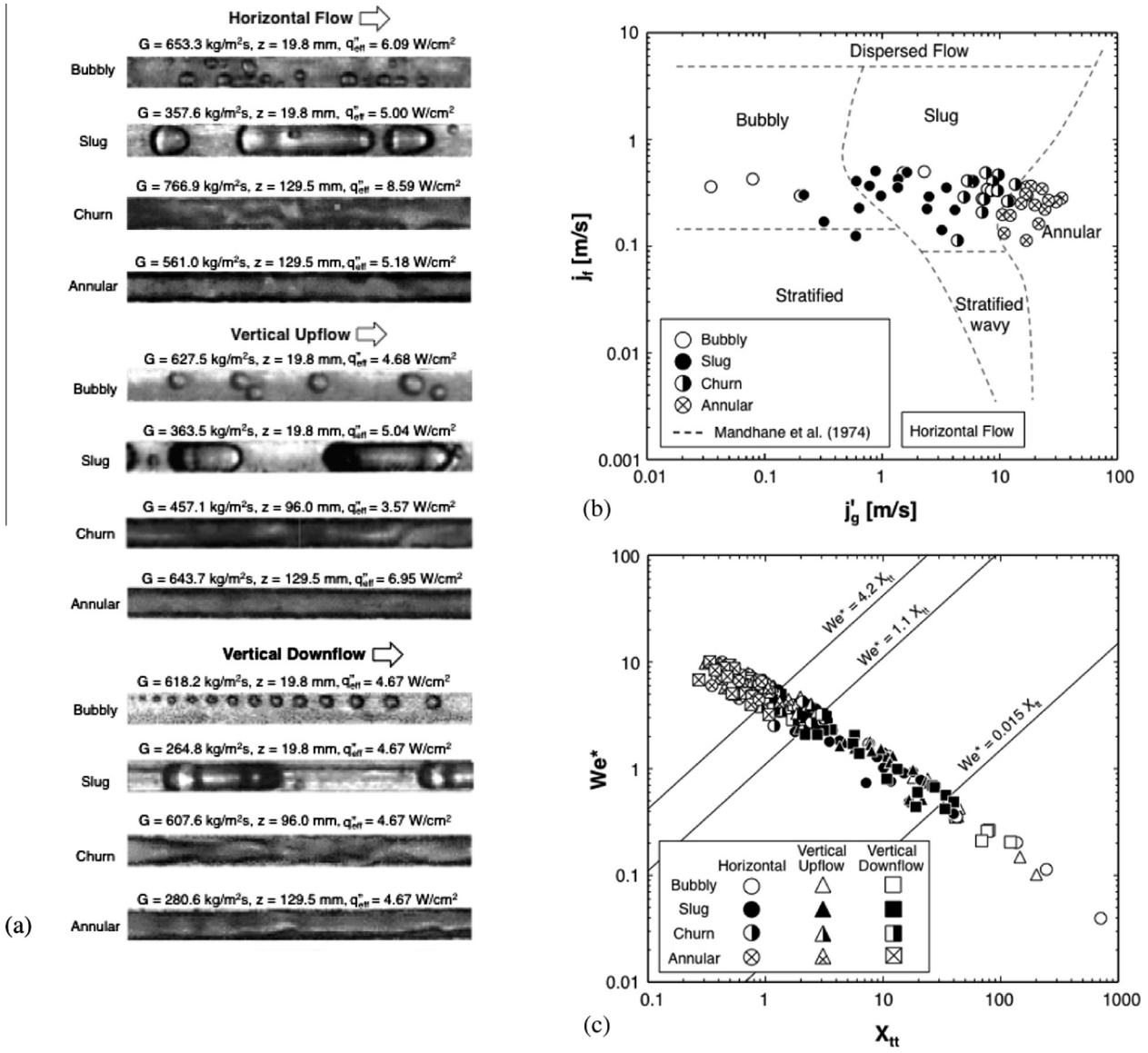

Fig. 13. (a) Images of representative flow regimes for different orientations, mass velocities and heat fluxes; the z values shown indicate central axial location for image. (b) Flow regime data compared to regime map based on jf versus $j'g$ for horizontal flow. (c) Flow regime data compared to regime map based on We^* versus X_{tt} for all three orientations.

the annular liquid film. These dimensionless parameters are defined as follows:

$$We^* = 2.45Re_g^{0.64}\left(\frac{\mu_g^2}{\rho_g\sigma D_h}\right)^{0.3}\Big/\phi_g^{0.4} \quad \text{for } \mathrm{Re}_f \le 1250, \tag{30a}$$

$$\text{and} \quad We^* = 0.85Re_g^{0.79}\left(\frac{\mu_g^2}{\rho_g\sigma D_h}\right)^{0.3}\left[\left(\frac{\mu_g}{\mu_f}\right)^2\left(\frac{\rho_f}{\rho_g}\right)\right]^{0.084}\left(\frac{X_{tt}}{\phi_g^{2.55}}\right)^{0.157} \quad \text{for } \mathrm{Re}_f > 1250, \tag{30b}$$

$$\text{where} \quad Re_g = xGD_h/\mu_g, \tag{31a}$$

$$Re_f = G(1-x)D_h/\mu_f, \tag{31b}$$

$$X_{tt} = \left(\frac{1-x}{x}\right)^{0.9}\left(\frac{\rho_g}{\rho_f}\right)^{0.5}\left(\frac{\mu_f}{\mu_g}\right)^{0.1}, \tag{32}$$

$$\text{and} \quad \phi_g = 1 + 1.09X_{tt}^{0.039}. \tag{33}$$

Fig. 13(c) uses the Soliman dimensionless parameters to segregate the present flow regime data for the three orientations. Like Fig. 13(b), the parameters used here are based on x and not x_e. There is appreciable clustering of data for different orientations indicating weak body force effects. Using simple linear We^* versus X_{tt} functions, transitions between the present flow regimes are well represented by the following.

$$\text{Bubbly to slug}: \quad We^* = 0.015X_{tt}. \tag{34a}$$

$$\text{Slug to churn}: \quad We^* = 1.1X_{tt}. \tag{34b}$$

$$\text{churn to annular}: \quad We^* = 4.2X_{tt}. \tag{34c}$$

4. Conclusions

This study explored the pressure drop and heat transfer characteristics of flow boiling in micro-channels for three different orientations. Experimental results for the different orientations are used to assess the influence of body force on two-phase heat transfer. By determining flow conditions that negate the influence of body

force for the different orientations, the study aims to develop similar criteria for reduced gravity and microgravity in space applications. Key findings from the study are as follows:

(1) The influence of orientation on two-phase heat transfer is significant for low mass velocities with $G/\rho_f < 0.22$ m/s, and negligible for $G/\rho_f > 0.22$ m/s. This demonstrates that, by using a sufficiently high mass velocity, flow boiling in micro-channels is highly effective at negating the influence of body force in space systems.
(2) Overall, pressure drop is dominated by two-phase friction followed, to a lesser degree, by two-phase acceleration and single-phase liquid friction. The contributions of inlet contraction and outlet expansion are mostly negligible.
(3) Two types of instability are encountered, mild parallel channel instability and severe pressure drop oscillation. The instabilities are exasperated with increasing heat flux and have a profound negative influence on the two-phase heat transfer coefficient.
(4) Four flow regimes are identified for all three orientations: bubbly, slug, churn and annular. The horizontal flow data show fair agreement with a previous map recommended specifically for horizontal flow. New simple dimensionless relations are developed for transition boundaries between the different regimes regardless of orientation.

Conflict of interest

None declared.

Acknowledgment

The authors are grateful for the support of the National Aeronautics and Space Administration (NASA) – United States under Grant no. NNX13AC83G.

References

[1] I. Mudawar, Two-phase micro-channel heat sinks: theory, applications and limitations, J. Electron. Packag. – Trans. ASME 133 (2011) 041002.
[2] C.Y. Han, P. Griffith, The mechanism of heat transfer in nucleate pool boiling, Int. J. Heat Mass Transfer 8 (1965) 887–903.
[3] P.J. Marto, V.J. Lepere, Pool boiling heat transfer from enhanced surfaces to dielectric fluids, J. Heat Transfer – Trans. ASME 104 (1982) 292–299.
[4] T.M. Anderson, I. Mudawar, Microelectronic cooling by enhanced pool boiling of a dielectric fluorocarbon liquid, J. Heat Transfer – Trans. ASME 111 (1989) 752–759.
[5] I. Mudawar, A.H. Howard, C.O. Gersey, An analytical model for near-saturated pool boiling CHF on vertical surfaces, Int. J. Heat Mass Transfer 40 (1997) 2327–2339.
[6] D.E. Maddox, I. Mudawar, Critical heat flux in subcooled flow boiling of fluorocarbon liquid on a simulated electronic chip in a rectangular channel, Int. J. Heat Mass Transfer 32 (1989) 379–394.
[7] T.C. Willingham, I. Mudawar, Forced-convection boiling and critical heat flux from a linear array of discrete heat sources, Int. J. Heat Mass Transfer 35 (1992) 2879–2890.
[8] H.J. Lee, S.Y. Lee, Heat transfer correlation for boiling flows in small rectangular horizontal channels with low aspect ratios, Int. J. Multiphase Flow 27 (2001) 2043–2062.
[9] Y. Katto, M. Kunihiro, Study of the mechanism of burn-out in boiling system of high burn-out heat flux, Bull. JSME 16 (1973) 1357–1366.
[10] M. Monde, T. Inoue, Critical heat flux in saturated forced convective boiling on a heated disk with multiple impinging jets, J. Heat Transfer – Trans. ASME 113 (1991) 722–727.
[11] D.C. Wadsworth, I. Mudawar, Enhancement of single-phase heat transfer and critical heat flux from an ultra-high-flux-source to a rectangular impinging jet of dielectric liquid, J. Heat Transfer – Trans. ASME 114 (1992) 764–768.
[12] M.E. Johns, I. Mudawar, An ultra-high power two-phase jet-impingement avionic clamshell module, J. Electron. Packag. – Trans. ASME 118 (1996) 264–270.
[13] S. Toda, A study in mist cooling (1st report: investigation of mist cooling), Trans. JSME 38 (1972) (1972) 581–588.
[14] L. Lin, R. Ponnappan, Heat transfer characteristics of spray cooling in a closed loop, Int. J. Heat Mass Transfer 46 (2003) 3737–3746.
[15] J.R. Rybicki, I. Mudawar, Single-phase and two-phase cooling characteristics of upward-facing and downward-facing sprays, Int. J. Heat Mass Transfer 49 (2006) 5–16.
[16] M. Visaria, I. Mudawar, Theoretical and experimental study of the effects of spray orientation on two-phase spray cooling and critical heat flux, Int. J. Heat Mass Transfer 51 (2008) 2398–2410.
[17] W. Nakayama, T. Nakajima, S. Hirasawa, Heat sink studs having enhanced boiling surfaces for cooling of microelectronic components, ASME Paper 84-WA/HT-89, 1984.
[18] R.L. Webb, The evolution of enhanced surface geometries for nucleate boiling, Heat Transfer Eng. 2 (1981) 46–69.
[19] V. Khanikar, I. Mudawar, T. Fisher, Effects of carbon nanotube coating on flow boiling in a micro-channel, Int. J. Heat Mass Transfer 52 (2009) 3805–3817.
[20] M.K. Sung, I. Mudawar, Experimental and numerical investigation of single-phase heat transfer using a hybrid jet-impingement/micro-channel cooling scheme, Int. J. Heat Mass Transfer 49 (2006) 682–694.
[21] I. Park, S. Kim, I. Mudawar, Experimental measurement and modeling of downflow condensation in a circular tube, Int. J. Heat Mass Transfer 57 (2013) 567–581.
[22] H. Lee, I. Mudawar, M.M. Hasan, Experimental and theoretical investigation of annular flow condensation in microgravity, Int. J. Heat Mass Transfer 61 (2013) 293–309.
[23] H. Zhang, I. Mudawar, M.M. Hasan, Experimental assessment of the effects of body force, surface tension force, and inertia on flow boiling CHF, Int. J. Heat Mass Transfer 45 (2002) 4079–4095.
[24] M. Saito, N. Yamaoka, K. Miyazaki, M. Kinoshita, Y. Abe, Boiling two-phase flow under microgravity, Nucl. Eng. Des. 146 (1994) 451–461.
[25] Y. Ma, J.N. Chung, An experimental study of forced convection boiling in microgravity, Int. J. Heat Mass Transfer 41 (1998) 2371–2382.
[26] Y. Ma, J.N. Chung, A study of bubble dynamics in reduced gravity forced-convection boiling, Int. J. Heat Mass Transfer 44 (2001) 399–415.
[27] H. Ohta, Experiments on microgravity boiling heat transfer by using transparent heaters, Nucl. Eng. Des. 175 (1997) 167–180.
[28] H. Zhang, I. Mudawar, M.M. Hasan, Flow boiling CHF in microgravity, Int. J. Heat Mass Transfer 48 (2005) 3107–3118.
[29] R.J. Simoneau, F.F. Simon, A visual study of velocity and buoyancy effects on boiling nitrogen, NASA Tech Note TN D-3354, 1966.
[30] K. Mishima, H. Nishihara, The effect of flow direction and magnitude on CHF for low pressure water in thin rectangular channels, Nucl. Eng. Des. 86 (1985) 165–181.
[31] C.O. Gersey, I. Mudawar, Effects of heater length and orientation on the trigger mechanism for near-saturated flow boiling critical heat flux – I. Photographic study and statistical characterization of the near-wall interfacial features, Int. J. Heat Mass Transfer 38 (1995) 629–641.
[32] C.O. Gersey, I. Mudawar, Effects of heater length and orientation on the trigger mechanism for near-saturated flow boiling critical heat flux – II. Critical heat flux model, Int. J. Heat Mass Transfer 38 (1995) 643–654.
[33] H. Zhang, I. Mudawar, M.M. Hasan, A method for assessing the importance of body force on flow boiling CHF, J. Heat Transfer – Trans. ASME 126 (2004) 161–168.
[34] C.R. Kharangate, I. Mudawar, M.H. Hasan, Experimental and theoretical study of critical heat flux in vertical upflow with inlet vapor void, Int. J. Heat Mass Transfer 55 (2012) 360–374.
[35] C.R. Kharangate, I. Mudawar, M.H. Hasan, Photographic study and modeling of critical heat flux in horizontal flow boiling with inlet vapor void, Int. J. Heat Mass Transfer 55 (2012) 4154–4168.
[36] C. Konishi, I. Mudawar, M.H. Hasan, Investigation of the influence of orientation on critical heat flux for flow boiling with two-phase inlet, Int. J. Heat Mass Transfer 61 (2013) 176–190.
[37] C. Konishi, I. Mudawar, M.H. Hasan, Criteria for negating the influence of gravity on flow boiling critical heat flux with two-phase inlet conditions, Int. J. Heat Mass Transfer 65 (2013) 203–218.
[38] H. Lee, I. Mudawar, M.M. Hasan, Flow condensation in horizontal tubes, Int. J. Heat Mass Transfer 66 (2013) 31–45.
[39] J.E. Galloway, I. Mudawar, CHF mechanism in flow boiling from a short heated wall – Part 2. Theoretical CHF model, Int. J. Heat Mass Transfer 36 (1993) 2527–2540.
[40] D.D. Hall, I. Mudawar, Ultra-high critical heat flux (CHF) for subcooled water flow boiling – II. High-CHF database and design parameters, Int. J. Heat Mass Transfer 42 (1999) 1429–1456.
[41] J.C. Sturgis, I. Mudawar, Critical heat flux in a long, rectangular channel subjected to one-sided heating – I. Flow visualization, Int. J. Heat Mass Transfer 42 (1999) 1835–1847.
[42] J.C. Sturgis, I. Mudawar, Critical heat flux in a long, rectangular channel subjected to one-sided heating – II. Analysis of CHF data, Int. J. Heat Mass Transfer 42 (1999) 1849–1862.
[43] D.D. Hall, I. Mudawar, Critical heat flux (CHF) for water flow in tubes – I. Compilation and assessment of World CHF data, Int. J. Heat Mass Transfer 43 (2000) 2573–2604.
[44] H. Lee, I. Park, I. Mudawar, M.M. Hasan, Micro-channel evaporator for space applications – 2. Assessment of predictive tools, Int. J. Heat Mass Transfer 77 (2014) 1231–1249.
[45] W. Qu, I. Mudawar, Flow boiling heat transfer in two-phase micro-channel heat sinks – I. Experimental investigation and assessment of correlation methods, Int. J. Heat Mass Transfer 46 (2003) 2755–2771.

[46] S.M. Kim, I. Mudawar, Consolidated method to predicting pressure drop and heat transfer coefficient for both subcooled and saturated flow boiling in micro-channel heat sinks, Int. J. Heat Mass Transfer 55 (2012) 3720–3731.
[47] G.E. Geiger, Sudden contraction losses in single and two-phase flow (Ph.D. thesis), University of Pittsburgh, PA, 1964.
[48] R.K. Shah, A.L. London, Laminar Flow Forced Convection in Ducts: A Source Book for Compact Heat Exchanger Analytical Data, Academic Press, New York, 1978 (Suppl. 1).
[49] F.P. Incropera, D.P. Dewitt, Fundamentals of Heat and Mass Transfer, fifth ed., Wiley, New York, 2002.
[50] W. Qu, I. Mudawar, Measurement and prediction of pressure drop in two-phase micro-channel heat sinks, Int. J. Heat Mass Transfer 46 (2003) 2737–2753.
[51] S. Levy, Forced convection subcooled boiling prediction of vapor volumetric fraction, Int. J. Heat Mass Transfer 10 (1967) 951–965.
[52] I. Mudawar, R.A. Houpt, Measurement of mass and momentum transport in wavy-laminar falling liquid films, Int. J. Heat Mass Transfer 36 (1993) 4151–4162.
[53] J.M. Mandhane, G.A. Gregory, K. Aziz, A flow pattern map for gas–liquid flow in horizontal pipes, Int. J. Multiphase Flow 1 (1974) 537–553.
[54] M.K. Dobson, J.C. Chato, Condensation in smooth horizontal tubes, J. Heat Transfer – Trans. ASME 120 (1998) 193–213.
[55] H.M. Soliman, Correlation of mist-to-annular transition during condensation, Can. J. Chem. Eng. 61 (1983) 178–182.